

JGR Space Physics

RESEARCH ARTICLE

10.1029/2019JA026787

Key Points:

- A new global MHD model is introduced for Jupiter's magnetosphere that self-consistently includes the Io plasma torus at the right location
- Time-dependent simulations show that the global magnetosphere responds differently to different types of drivers in the solar wind
- Plasmoids form in the tail with occurrence frequency dependent on the external driving

Correspondence to:

Y. Sarkango,
sarkango@umich.edu

Citation:

Sarkango, Y., Jia, X., & Toth, G. (2019). Global MHD simulations of the response of Jupiter's magnetosphere and ionosphere to changes in the solar wind and IMF. *Journal of Geophysical Research: Space Physics*, 124, 5317–5341. <https://doi.org/10.1029/2019JA026787>

Received 1 APR 2019




Accepted 16 JUN 2019

Accepted article online 30 JUL 2019

Published online 16 JUL 2019

©2019. American Geophysical Union.
All Rights Reserved.

Global MHD simulations of the Response of Jupiter's Magnetosphere and Ionosphere to Changes in the Solar Wind and IMF

Yash Sarkango¹ , Xianzhe Jia¹ , and Gabor Toth¹ 

¹Department of Climate and Space Sciences and Engineering, University of Michigan, Ann Arbor, MI, USA

Abstract We have developed a new global magnetohydrodynamic (MHD) model for Jupiter's magnetosphere based on the BATSRUS code and an ionospheric electrodynamics solver. Our model includes the Io plasma torus at its appropriate location and couples the global magnetosphere with the planetary ionosphere through field-aligned currents. Through comparisons with available particle and field observations as well as empirical models, we show that the model captures the overall configuration of the magnetosphere reasonably well. In order to understand how the magnetosphere responds to different solar wind drivers, we have carried out time-dependent simulations using various kinds of upstream conditions, such as a forward shock and a rotation in the interplanetary magnetic field (IMF). Our model predicts that compression of the magnetosphere by a forward shock of typical strength generally weakens the corotation enforcement currents on the dayside and produces an enhancement on the nightside. However, the global response varies depending on the IMF orientation. A forward shock with a typical Parker-spiral IMF configuration has a larger impact on the magnetospheric configuration and large-scale current systems than with a parallel IMF configuration. Plasmoids are found to form in the simulation due to tail reconnection and have complex magnetic topology, as they evolve and propagate down tail. For a fixed mass input rate in the Io plasma torus, the frequency of plasmoid occurrence in our simulation is found to vary depending on the upstream solar wind driving.

1. Introduction

The gas giants, Jupiter and Saturn, both possess a strong internal magnetic field like Earth, but the relatively fast planetary rotation and the presence of significant internal sources of plasma lead to vastly different magnetospheric configurations and dynamics compared to the terrestrial magnetosphere (Khurana et al., 2004; Krupp et al., 2004, and references therein). The internal sources of plasma at the giant planets are supplied predominantly by their moons, Io at Jupiter (Bolton et al., 2015, and references therein) and Enceladus at Saturn (Blanc et al., 2015, and references therein). In particular at Jupiter, through ionization of its volcanically erupted neutral particles, Io supplies heavy ions at a rate of ~250–1,000 kg/s to the magnetosphere (Bagenal & Delamere, 2011). This leads to a high-density plasma sheet that is forced to corotate with the planet to large radial extents (~20–30 R_J) by the corotation enforcement current system composed of radial currents in the equatorial plane, field-aligned currents that couple the magnetosphere to the ionosphere and Pedersen currents in the ionosphere (Cowley et al., 2003; Cowley & Bunce, 2001; Hill, 1979, 1980, 2001; Vasyliunas, 1983). In studying the complex spatial form and temporal variability of Jovian aurora, it is typically subdivided into three components—main emission (oval), polar emissions, and equatorward emissions. The main oval of the Jovian aurora is thought to be at the location in the ionosphere where upward field-aligned currents associated with the corotation enforcement current system are present (Cowley & Bunce, 2001; Hill, 2001; Southwood & Kivelson, 2001). Theoretical models have predicted that a compression of the magnetosphere due to an increase in solar wind dynamic pressure would lead to a reduction of the main auroral oval intensity on the dayside (Cowley & Bunce, 2003; Cowley & Nichols, 2007; Southwood & Kivelson, 2001). Subcorotating plasma in the dayside equatorial magnetosphere would speed up in the azimuthal direction as the magnetosphere is compressed due to conservation of angular momentum, thereby decreasing the strength of the corotation enforcement current at this location, which in turn would dim the Jovian main aurora. Using a global magnetohydrodynamic (MHD) model, Chané et al. (2017) found that while the nightside/flank currents in the ionosphere are enhanced due to a simulated forward shock, the dayside currents are weakened, which is consistent with the previous theoretical prediction.

Although the Jovian ultraviolet (UV) aurora is well structured and always present, remote observations made by the Hubble Space Telescope (HST) and Hisaki/EXCEED observations of the Jovian UV aurora have shown that its intensity is highly variable and is often correlated with the dynamic pressure of the upstream solar wind (Clarke et al., 2009; Kimura et al., 2015, 2018; Kita et al., 2016; Nichols et al., 2007, 2017). Due to lack of a dedicated solar wind monitor at Jupiter, identifying the correlation between changes in the auroral emissions and upstream parameters typically requires a numerical model, typically a 1-D MHD model (Tao et al., 2005; Zieger & Hansen, 2008), to propagate the solar wind from 1 AU to Jupiter's orbit, which is subject to timing errors due to assumptions made in the model and the orbital geometry/alignment of Jupiter relative to available solar wind monitors at 1 AU. Exceptions to this situation include Cassini's flyby of Jupiter and Juno's approach orbit, during which in situ measurements of the solar wind and remote observations of the Jovian aurora could be made simultaneously (Gurnett et al., 2002; Nichols et al., 2007, 2017). Gurnett et al. (2002) report an event where Cassini observed an interplanetary shock a few hours prior to a large increase in UV emission intensity from Jupiter. Recently, Nichols et al. (2017) report observations made by HST during Juno's approach to Jupiter, during which the Juno spacecraft detected a large increase in solar wind dynamic pressure (Wilson et al., 2018), which resulted in intensification of the main emission in UV, observed by both HST and the Hisaki spacecraft (Kimura et al., 2017).

Intensities of the polar emissions are comparable to those of the main emission (Grodent et al., 2003); however, unlike the main emission, they do not have a steady morphology and are highly variable. UV observations made by HST have shown that the polar aurora contains highly dynamic regions with different repeating patterns such as "swirls" (in the swirl-region), "arcs," and "patches" (in the dusk active region) and occasional "filaments" (Bonfond et al., 2017; Grodent, 2015; Grodent et al., 2003; Nichols et al., 2009). Due to the complex rotationally driven dynamics of the Jovian magnetosphere (Vasyliunas, 1983), it is unclear how much open flux is typically present in the Jovian polar regions, and which features of the polar aurorae map to open field lines in the solar wind as opposed to processes in the outer magnetosphere or magnetotail (Cowley et al., 2003). Some models argue that Jupiter's magnetosphere is largely closed (McComas & Bagenal, 2007), since the reconnected field lines may undergo successive reconnection during the time it takes to travel through the magnetosphere, while other studies predict that Jupiter's magnetosphere does contain appreciable amount of open flux (Cowley et al., 2008; Masters, 2017; Vogt et al., 2011) and that the Dungey cycle (Dungey, 1961) and the Vasyliunas cycle coexist to influence the structure and dynamics of Jupiter's magnetosphere.

Global MHD models provide a useful tool for investigating these large-scale magnetospheric phenomena and can help answer those questions related to magnetospheric configuration discussed above. Many attempts to model Jupiter's magnetosphere have been made trending toward increasing degree of complexity—starting from Miyoshi and Kusano (1997), followed by the MHD model of Ogino et al. (1998), which was used in multiple studies to model the Jovian bow shock and magnetopause (Joy et al., 2002) and to study magnetospheric currents and the solar wind-magnetosphere interaction (Walker et al., 2001). Fukazawa et al. (2006) improved upon the model of Ogino et al. (1998) and investigated the dynamics of the magnetosphere such as the location, frequency of occurrence and characteristics of tail reconnection and plasmoid formation (Fukazawa et al., 2010). Moriguchi et al. (2008) studied magnetospheric currents using their global MHD model. Chané et al. (2013) developed an MHD model and used it to study the influence of mass loading due to Io on the magnetosphere. In subsequent studies, Chané et al. (2017, 2018) investigated the response of the magnetosphere to changes in the solar wind (specifically increases in solar wind dynamic pressure) and its influence on field-aligned currents in the ionosphere, which is directly relevant to this study. Recently, Wang et al. (2018) have also developed an MHD model for Jupiter's magnetosphere. However, placing the inner boundary of the MHD simulation nearer to the planet increases the computational cost, forcing MHD models to either place the mass loading sources at an unrealistic location well outside the orbit of Io or neglect mass loading altogether and introduce mass loading using a prescribed boundary condition at the inner boundary.

In this work we introduce a new MHD model for Jupiter's magnetosphere based on the BATSRUS MHD code (Powell et al., 1999; Gombosi et al., 2002), which is coupled to the Ridley ionosphere Poisson solver (Ridley et al., 2004). Unlike previous MHD models, our model includes mass loading due to Io in a self-consistent manner at the right location. Using the MHD model, we investigate in detail the time-dependent global response of the Jovian magnetosphere to different types of solar wind disturbances, such as

interplanetary shocks and the rotation of the interplanetary magnetic field (IMF). We analyze the response of the corotation enforcement current system to these upstream changes. Through our model we also identify closed and open field line regions in the northern hemisphere and southern hemisphere of Jupiter to understand the magnetic topology associated with the release of plasmoids and other dynamical processes.

In section 2 we describe the basics of global MHD model and highlight the important features that make this model well suited for simulating Jupiter's magnetosphere. In section 3 we provide validation of the MHD model by comparing simulation results with available in situ observations. In section 4 we present results from different simulations in which the upstream parameters are varied in order to investigate the response of the magnetosphere and current systems to changes in the external conditions, whereas in section 5 we show the corresponding response in the ionosphere. Section 6 shows an analysis of the variation of the open flux and reconnection-driven dynamics in the Jovian magnetosphere.

2. Model Description

Our MHD model for Jupiter's magnetosphere utilizes the Space Weather Modeling Framework (SWMF) developed at the University of Michigan (Tóth et al., 2012) and is an extension of the model used by Hansen (2001). Two modules of the SWMF are used—a magnetospheric solver that employs BATSRUS (Gombosi et al., 2002; Powell et al., 1999), and a Poisson solver for the ionospheric electrostatics (IE; Ridley et al., 2004), and the two modules are two-way coupled through the SWMF. In this work we use the single-fluid, semirelativistic version of BATSRUS, which solves the ideal MHD equations using a finite-volume approach. Details about the implementation of BATSRUS and the equations solved in this study can be found in Gombosi et al. (2002) and Tóth et al. (2012). The maximum wave speed allowable by the semirelativistic equations is the speed of light (Gombosi et al., 2002); however, we employ the Boris correction that artificially decreases this speed by a factor of 0.1 to allow for larger time steps (Tóth et al., 2011). Two-way coupling between BATSRUS and the IE solver is achieved in the following manner. Field-aligned currents from the magnetosphere are collected at a prescribed radial distance of $3 R_J$ ($R_J = 71,492$ km is Jupiter's mean radius) and are mapped to the surface of the planet assuming that the magnetic field between 1 and $3 R_J$ is dipolar. At the surface, a Poisson solver is used to solve Ohm's law for a given distribution of ionospheric conductance. In the present work, we assume a uniform Pedersen conductance of 0.05 S, which is on the lower end of previous estimates (0.1–10 S by Strobel & Atreya, 1983, and Nichols & Cowley, 2003) and set the Hall conductance to 0. The perturbation electric field obtained from the IE module is added to the corotational electric field, and the total electric field is then used to prescribe the plasma velocity at the inner boundary of the MHD domain at $2.5 R_J$. A detailed discussion of how this coupling is achieved is given by Ridley et al. (2004) in the context of the terrestrial magnetosphere and by Jia, Hansen, et al., 2012; Jia, Kivelson, et al., 2012) in application to Saturn's magnetosphere. The planetary magnetic field currently used in our model is an axisymmetric dipole with an equatorial surface field strength of 428,000 nT, and the rotation period of the planet is set to be 9.9 hr.

Our three-dimensional magnetospheric simulation domain spans a spherical region of $1,800 R_J$ centered at Jupiter, along with a planar cut at $X = +192 R_J$ that serves as the upstream boundary (Figure 1). The radial spacing between the grid cells increases in a logarithmic manner allowing for finer cells placed in regions close to the planet. The simulation domain is subdivided into a number of blocks (Powell et al., 1999), which can be refined independently to obtain the desired grid resolution in regions of interest, such as the equatorial magnetosphere, the magnetopause boundary, and the magnetotail. Although BATSRUS allows for physics criteria-based adaptive grid refinements (Tóth et al., 2012), in our simulations the refinements are prescribed initially and are fixed. The spherical inner boundary of our simulation domain is located at $2.5 R_J$, which then allows us to include the Io plasma torus centered at $\sim 5.9 R_J$ at the appropriate location. We specifically chose to refine a torus-like region near Io's orbit for accurately modeling the mass loading processes occurring in the Io plasma torus. The smallest radial grid spacing is $\sim 0.06 R_J$, which is present in the Io plasma torus. Figure 1 shows our simulation grid with contours of simulated plasma density shown in the background for context. The relatively coarse grids near the polar regions of the planet were chosen to allow for larger time steps in order to increase the speed of the simulation, as these regions contain strong magnetic fields and thus high wave speeds as well as small grid cells due to the convergence of the spherical grid near the Z axis.

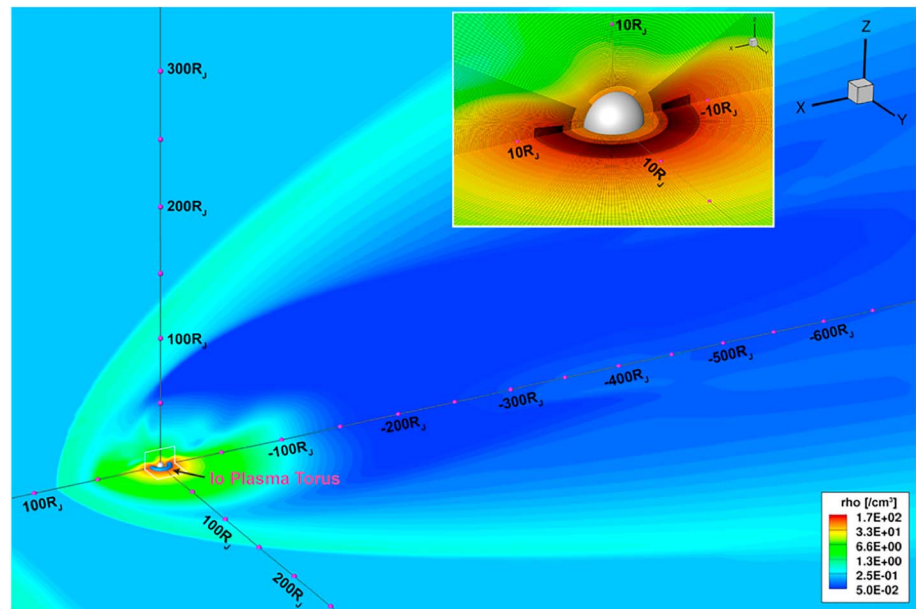


Figure 1. A global view of our Jupiter global magnetohydrodynamic model. Color contours of modeled plasma density are shown in the equatorial and noon-midnight meridional planes. The blue isosurface around Io's orbit at $\sim 5.9 R_J$ shows the plasma torus included in the model. The inset shows the high-resolution spherical grid adopted to resolve the mass loading processes in the Io plasma torus.

All MHD variables at the upstream boundary at $x = 192 R_J$ are prescribed on account of the super-Alfvénic and supersonic flow, whereas floating boundary conditions that set zero gradients for all MHD variations are applied at the outer boundary in the downstream direction (located at $-1,800 R_J$). At the inner boundary at $2.5 R_J$, we fixed the plasma density at 50 amu/cm^3 and set the magnetic field and plasma pressure to float. Using the electrostatic potential calculated by the IE Poisson solver, we calculate the electric field at the inner boundary. The $\mathbf{E} \times \mathbf{B}$ velocity thus obtained is added to the corotation velocity ($\mathbf{v} = -\boldsymbol{\omega} \times \mathbf{r}$) at the inner boundary.

The fluxes at cell interfaces used in the finite-volume method are calculated using a second-order accurate implementation of Linde's HLL scheme (Linde, 2002). To achieve computational speeds feasible for running long-duration simulations, we employ a hybrid time-stepping scheme. Explicit time-stepping methods are subject to the Courant-Friedrichs-Lewy criterion that imposes a stringent constraint on the allowable time step, which may become rather small in regions of high wave speeds, such as the polar region near the planet. Implicit time-stepping schemes are unconditionally stable and therefore allow larger time steps but involve matrix inversion, which can be computationally expensive for large systems. To combine the strengths of these two methods, we use a “explicit/implicit” time-stepping algorithm developed by Tóth et al. (2006). Since our domain is divided into grid blocks, with each block containing $6 \times 8 \times 8$ cells, this algorithm allows for each block to be solved using either explicit or implicit time stepping for a prescribed value of the computational time step. Blocks in which all cells abide by the *Courant-Friedrichs-Lewy* criterion defined for the time step are solved using explicit time stepping. In total, our finite-volume grid contains approximately 19 million cells, and with a 20-s time step our global model can achieve almost real-time performance using $\sim 2,000$ cores on National Aeronautics and Space Administration's supercomputer Pleiades.

In order to accurately model Jupiter's magnetosphere, it is necessary to include the contribution of plasma by its moons, especially Io. Io provides the largest internal source of plasma to Jupiter's magnetosphere, estimated to add $\sim 250 \text{ kg/s}$ to 1 ton/s of plasma (Bagenal & Delamere, 2011). In our model, we include contributions due to ionization and charge-exchange in the form of source terms in the mass, momentum, and energy equations. Electron recombination is assumed to be a minor process and, therefore, neglected in the present simulations. We use a prescribed neutral torus centered at Io's orbital radius of $5.9 R_J$ according to the following form. The neutral distribution used for the Io torus is a modified form of the one obtained by

Schreier et al. (1998) and an exponential falloff with latitude is considered. We use the following expression to calculate the neutral number density (n_n [cm^{-3}]) at a spatial location ($r_{xy} = \sqrt{x^2 + y^2}$, z) R_J .

$$n_n(r_{xy}, z) = n_{n0} \exp\left(\frac{-z^2}{H_s^2}\right) \times \begin{cases} 60 \times \exp\left(\frac{r_{xy} - 5.71}{0.2067}\right) & ; r_{xy} < 5.71 \\ 60 \times \exp\left(\frac{-r_{xy} + 5.685}{0.1912}\right) & ; 5.71 < r_{xy} < 5.875 \\ 19.9 \times \exp\left(\frac{-r_{xy} + 5.9455}{0.0531r_{xy} + 0.5586}\right) & ; r_{xy} > 5.875 \end{cases}$$

where the scale height is chosen to be $H_s = r_{xy} \tan^{-1} 2.5^\circ$. New ions are produced from the above neutral distribution by multiplying with a constant ionization rate and collision cross section based on the following expression for the net plasma production rate per unit volume (units of $\text{kg}\cdot\text{m}^{-3}\cdot\text{s}^{-1}$):

$$\dot{\rho} = 16 m_p n_n C_i$$

Here C_i is the ionization rate (specified to 10^{-4} s^{-1} in our simulations) and 16 amu is taken to be the average mass of the heavy ions present in Jupiter's magnetosphere. With this information, we construct the source term \vec{S} for the mass continuity, momentum, total energy and thermal energy equations (Hansen, 2001):

$$\begin{aligned} S_\rho &= \dot{\rho} - \alpha_{\text{rec}} \rho \\ S_{\rho U_x} &= (\dot{\rho} - C_{cx}) u_{nx} - (C_{cx} + \alpha_{\text{rec}}) \rho u_x \\ S_{\rho U_y} &= (\dot{\rho} - C_{cx}) u_{ny} - (C_{cx} + \alpha_{\text{rec}}) \rho u_y \\ S_{\rho U_z} &= -(C_{cx} + \alpha_{\text{rec}}) \rho u_z \\ S_E &= \frac{1}{2} (\dot{\rho} + C_{cx} \rho) u_n^2 - \frac{1}{2} \rho u^2 (C_{cx} - \alpha_{\text{rec}}) + \frac{3}{2} p + \frac{3}{2} C_{cx} p \\ S_P &= \frac{1}{2} (\dot{\rho} + C_{cx} \rho) |\vec{u} - \vec{u}_n|^2 - \frac{3}{2} \alpha_{\text{rec}} p \end{aligned}$$

where $C_{cx} = \dot{\rho} - n_n \sigma |\vec{u} - \vec{u}_n|$ is the charge-exchange rate, \vec{u}_n is the Keplerian velocity of neutral particles orbiting Jupiter, and α_{rec} is the recombination rate, which is set to 0 in our current work.

As described above, the ion production rate in our simulation is a controlled parameter depending on the neutral profile, ionization rate, and collision cross section. In the present work, we set the total ion production rate of ~ 1 ton/s. Figure 2 shows a contour plot in the meridional plane of the mass loading profile used. It is important to note that our approach of modeling the Io plasma torus is very different from those adopted by the previous Jupiter global MHD models. For instance, the Miyoshi and Kusano (1997) MHD model had its inner boundary at $30 R_J$. The inner boundary of the MHD model by Ogino et al. (1998) and Fukazawa et al. (2005), Fukazawa et al., (2006, 2010) lied at $15 R_J$, while the Moriguchi et al. (2008) model had its inner boundary at $8 R_J$. The recent MHD model by Chané et al. (2013, 2017) used an extended ionospheric region spanning from 4.5 to $8.5 R_J$ and placed the Io torus at an unrealistic location of $10 R_J$. In their recent model, Wang et al. (2018) also chose to place the Io torus at $10 R_J$ for the same reasons. Our model is the first global MHD model which models mass loading due to Io in a self-consistent manner at the right location.

We note that the global simulations presented here are based on an ideal MHD model, which does not capture nonideal MHD processes, such as energy-dependent particle drifts, temperature anisotropy, and kinetic physics involved in magnetic reconnection. While no simulation can fully model the complexity of a planetary magnetosphere, extensive prior work has demonstrated that MHD models generally can provide a reasonably good representation of the global structure of a planetary magnetosphere whose size is much larger than the characteristic ion spatial scales, which is the case for Jupiter. This is true, because while magnetic reconnection occurs due to numerical resistivity in the model, it generally occurs at the right location where the current sheets carry strong currents (numerically represented by a jump in the magnetic field) and approximately with the correct reconnection rate that is some fraction ~ 0.1 of the Alfvén speed (the numerical diffusion term is proportional with the local maximum wave speed); therefore, the global solution is

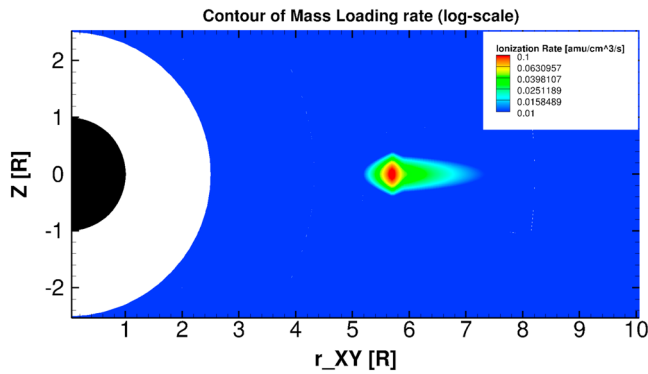


Figure 2. Contour plot showing the distribution of the ionization rate (centered at Io’s orbital location of $5.9 R_J$) in the XZ plane used in our simulation. The black disk represents Jupiter, and the white disk shows the simulation inner boundary at $2.5 R_J$.

expected to be approximately right. The main goal of this study is to investigate the large-scale response of Jupiter’s coupled magnetosphere-ionosphere system to solar wind drivers, for which an MHD model is a suitable tool.

3. Magnetospheric Configuration and Model Validation

To create the magnetosphere, we use steady solar wind conditions with a southward (negative B_Z) IMF (values are given in column 1 of Table 1) to minimize reconnection at the start of the simulation. We speed up the creation of the magnetosphere by using local time stepping (Tóth et al., 2012) for 50,000 iterations and then switch to time-accurate mode for 150 hr to produce a quasi-steady state magnetosphere. All simulations presented in this paper have been started either from this point or a later time step. Because of the large system size and long time scales involved in Jupiter’s global magnetosphere, it appears necessary to adopt the procedure described above in order to ensure that simulation results shown and discussed here are not from a period dominated by the initial transients.

Following the procedure described above, we have conducted a series of global simulations with different sets of upstream conditions given in Table 1. In this work, we are interested in understanding how the global magnetospheric configuration varies depending on the solar wind and IMF conditions. Therefore, we first run the simulation using fixed nominal solar wind parameters but with two different IMF orientations: Run 1 with a purely southward (parallel to Jupiter’s magnetospheric field) IMF to minimize effects of day-side magnetopause reconnection and Run 3, with the IMF in east-west direction representative of the typical Parker spiral configuration at Jupiter. For each of the two IMF orientations, we perform two additional simulations (Runs 2 and 4) in which we introduce a solar wind dynamic pressure enhancement to study the response of Jupiter’s magnetosphere to impact of interplanetary shocks.

To validate our global simulation model, we first present a set of comparisons of our MHD model results with available empirical models and in situ measurements. Figure 3 shows a snapshot of the magnetospheric configuration in the equatorial (XY) plane extracted from the simulation using fixed nominal solar wind conditions and a southward IMF (Run 1 in Table 1) after it has reached quasi-steady state. Results are presented in a Jupiter-centered Cartesian coordinate system, where X points toward the Sun, Z is the magnetic and rotational axis (since dipole tilt is ignored), and Y completes the right-handed coordinate system. The colors show contours of plasma density in logarithmic scale. The magenta points in the equatorial plane are the extracted equatorial footprints of the last closed field lines, which, on the dayside, correspond to the magnetopause in our model. The bow shock in our model can be readily identified as the separatrix between the unperturbed solar wind and the magnetosheath containing high-density plasmas. Also plotted are the 25% and 75% probability curves from the Joy et al. (2002) magnetopause and bow shock models assuming the

duration of simulation (hours) 400 100 150 100
 n (cm^{-3}) 0.2 0.2 \rightarrow 0.5463 0.2 0.2 \rightarrow 0.5463
 \vec{B} (nT) (0, 0, -1) (0, 0, -1) \rightarrow (0, 0, -2.82) (0, 0, -1) \rightarrow (0, 1, 0) (0, 1, 0) \rightarrow (0, 2.82, 0)
 \vec{u} (km/s) (-400, 0, 0) (-400, 0, 0) \rightarrow (-532.47, 0, 0) (-400, 0, 0) (-400, 0, 0) \rightarrow (-532.47, 0, 0)
 Dynamic pressure (nPa) 0.053 0.053 \rightarrow 0.258 0.053 0.053 \rightarrow 0.258

Table 1
Upstream Solar Wind and IMF Conditions Used for the Simulations

	Run 1 No change in initial conditions (continued from steady state)	Run 2 Dynamic pressure enhancement with southward IMF (continued midway from Run 1)	Run 3 IMF turning from southward to Parker-spiral (continued midway from Run 1)	Run 4 Dynamic pressure enhancement with Parker-spiral IMF (continued from Run 3)
Duration of Simulation (hours)	400	100	150	100
n (cm^{-3})	0.2	0.2 \rightarrow 0.5463	0.2	0.2 \rightarrow 0.5463
\vec{B} (nT)	(0, 0, -1)	(0, 0, -1) \rightarrow (0, 0, -2.82)	(0, 0, -1) \rightarrow (0, 1, 0)	(0, 1, 0) \rightarrow (0, 2.82, 0)
\vec{u} (km/s)	(-400, 0, 0)	(-400, 0, 0) \rightarrow (-532.47, 0, 0)	(-400, 0, 0)	(-400, 0, 0) \rightarrow (-532.47, 0, 0)
Dynamic pressure (nPa)	0.053	0.053 \rightarrow 0.258	0.053	0.053 \rightarrow 0.258

Note. IMF = interplanetary magnetic field.

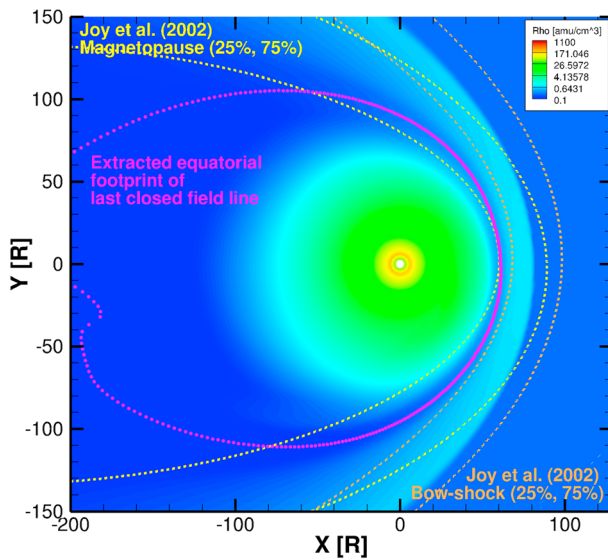


Figure 3. Density contours are shown in log scale for the equatorial plane. Overlaid are the 25–75% probability lines from the Joy et al. (2002) magnetopause and bow shock model, shown by dashed lines (yellow = magnetopause and orange = bow shock). Also shown in magenta are the equatorial crossings of the last closed field line, which corresponds to the magnetopause on the dayside (for $x > 0$).

same upstream solar wind pressure as used in our simulation. The comparison shows that the modeled magnetopause and bow shock fall well within the ranges predicted by the Joy et al. empirical model. It is, however, worth noting that while the modeled magnetospheric boundaries, in general, have a good agreement with observations, the size of the magnetosphere is slightly underestimated, due in part to absence of energetic particle pressure in our MHD model.

As another step in our model validation, we compare in Figure 4 the radial distribution of simulated plasma parameters with available in situ observations. In analyzing our simulation output, it became clear to us that the magnetosphere exhibits strong local time asymmetries and temporal variabilities. Therefore, in order to obtain a fair comparison with satellite data, which were collected in different local time sectors and in different magnetospheric states, we extracted simulation outputs in different local time meridians (LT = 0, 6, 12, and 18) and also from different time steps that cover both the southward (Run 1) and spiral IMF (Run 3) cases. Figure 4a shows the time-averaged radial profiles of the simulated plasma density in the central plasma sheet (blue/cyan curves), in comparison with a compilation of density profiles obtained from previous missions (adapted from Bagenal & Delamere, 2011). The density in the inner magnetosphere (inside $\sim 10 R_J$) are significantly underestimated in our simulation, whereas it matches the observations in the middle and outer magnetosphere ($> 10 R_J$) generally well. Several factors may contribute

to the discrepancy seen in the inner magnetosphere. For instance, the grid resolution in the torus region, albeit relatively fine, may not be high enough to resolve the small scale height associated with the torus. Moreover, plasma pressure is assumed to be isotropic in our ideal MHD model, but anisotropies in plasma pressure may develop in regions where ion pickup occurs, for example, in the torus. Pressure anisotropies ($P_{\perp} > P_{\parallel}$) would cause the plasma to be more confined to the centrifugal equator (e.g., as discussed by Dougherty et al., 2017). However, because of the isotropic pressure assumption in our current ideal MHD model, the modeled plasma sheet in the inner magnetosphere is thicker than observed, which contributes to the underpredicted densities near the equator as shown in Figure 4a.

Figure 4c shows a comparison of our modeled plasma pressure with the Galileo Plasma Science (PLS) measurements (Frank et al., 2002). Again, our model predicts lower pressures than observed in the inner magnetosphere, because of the lower densities discussed above. Nevertheless, the modeled pressure has a satisfactory agreement with the observations in the middle and outer magnetosphere ($> \sim 15 R_J$). Figure 4d compares our modeled plasma β with Galileo observations (Mauk et al., 2004). The observations show that the plasma β is < 1 in the inner magnetosphere and > 1 in the middle/outer magnetosphere, and it crosses unity around $15 R_J$. Our model results show a very similar general trend, although our modeled plasma β tends to be lower than the observations due to the underestimation of density and absence of energetic particle pressure. However, in the middle and outer magnetosphere, our simulated β appears to have a good agreement with the observations, especially in the nightside region. Our model also suggests that there is a considerable variability in the plasma β among different local time sectors (largest near the midnight sector and smallest near noon sector), which is important to consider when it comes to model-data comparison.

Figure 4b presents a validation of the plasma azimuthal velocity. The radial profile of the azimuthal velocity provides important constraints on models of plasma transport and magnetosphere-ionosphere coupling, as demonstrated by a number of previous studies (e.g., Cowley & Bunce, 2001; Hill, 1979, 1980; Nichols, 2011; Nichols & Cowley, 2004; Pontius, 1997). The observations show that the plasma flow starts to deviate significantly from rigid corotation around $20 R_J$, where the corotation enforcement currents start to develop (e.g., Cowley & Bunce, 2001; Hill, 2001). In comparison, our modeled flow profiles show a very similar behavior in that the corotation breakdown occurs at about $15\text{--}20 R_J$, in general agreement with the observations. The simulated azimuthal flows in all local time sectors are subcorotating outside of $\sim 20 R_J$, with a strong dependence on local time varying between 150 and 210 km/s at $\sim 30 R_J$, which may account for the relatively large

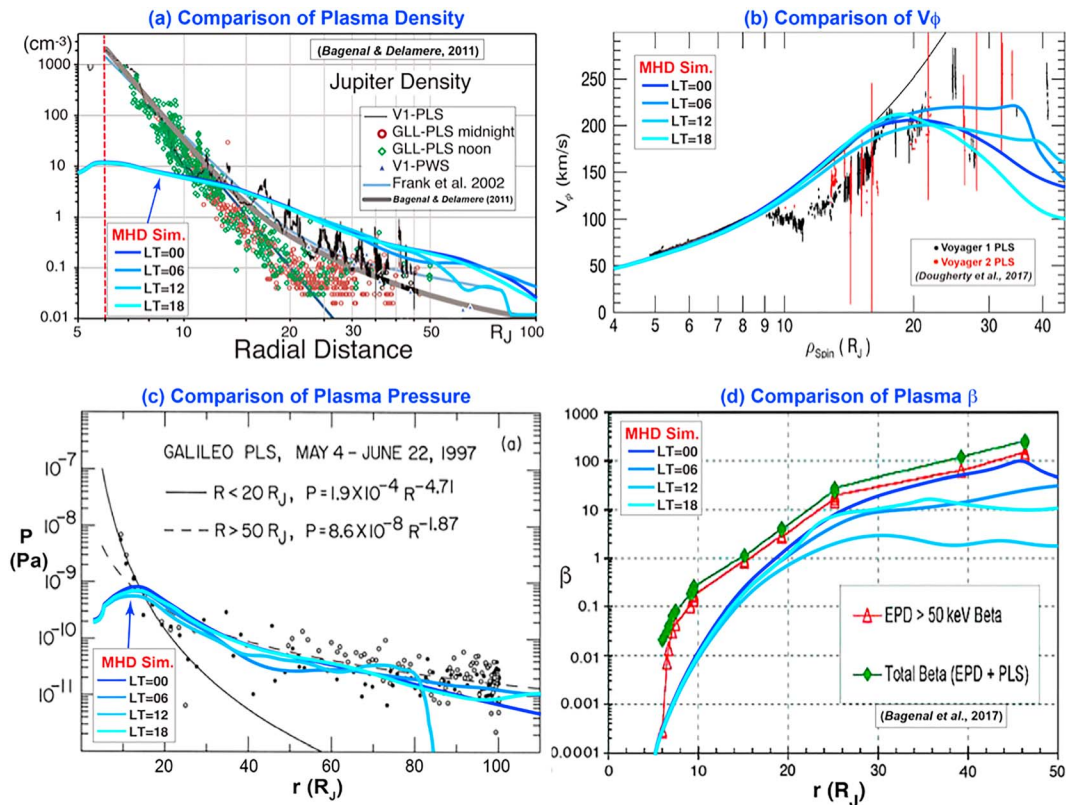


Figure 4. Comparisons of the plasma parameters between our global MHD model and observations. In each panel, there are four traces extracted from the MHD model representing the radial profiles at four different local times (LT = 00, 06, 12, 18). (a) Plasma density. The compilation of density profiles based on Voyager and Galileo measurements is adapted from Bagenal and Delamere (2011). (b) Plasma azimuthal velocity (V_ϕ). Voyager 1 and Voyager 2 PLS data are shown as black and red dots (with error bars; adapted from Dougherty et al., 2017). The black curve shows the rigid corotation speed for reference. (c) Plasma thermal pressure. The circles show the plasma pressures measured by Galileo PLS, while the black solid and dashed curves show fits to the data (adapted from Frank et al., 2002). (d) Plasma β . The red symbols and lines show the β that only includes Galileo EPD-measured energetic particle pressure contribution, whereas the green symbols and lines show the total β when both EPD and PLS measured pressures are included (adapted from Mauk et al., 2004). EPD = energetic particles detector; MHD = magnetohydrodynamic; GLL-PLS = Galileo Plasma Science Investigation.

scattering of the measured flow velocities in this region. One feature in the observations that is not captured by our model is the deviation of the plasma flow from rigid corotation between ~ 9 and $15 R_J$. Plasma subcorotation in this region so deep inside the magnetosphere was not predicted in the previous theoretical and numerical models. The physical cause of this behavior remains unidentified at present, and requires further investigation.

In addition to the plasma parameters, we also compare our simulated magnetic field with observations. As an example, Figure 5 presents a comparison of the magnetic field component normal to the current sheet (B_N) to the data collected by previous missions, including Pioneer, Voyager, Ulysses, and Galileo (Vogt et al., 2011). This data set was the basis of the magnetic field model (fits to the data shown as blue curves in the figure) developed by Vogt et al. (2011) that allows to map regions in the magnetosphere to the ionosphere. The observational data were shown in different local time bins; thus, we extracted our model results from the same local time sectors correspondingly. Since there are time-varying structures formed in our simulation even under steady upstream conditions, we show both the time-averaged radial profiles and the range of B_N seen in our simulation. Overall, our model result follows the trends of the B_N variation quite well in all local time sectors compared. Comparing the ranges of our modeled B_N with the data also shows that much of the scattering in the data could potentially be attributed to temporal variations of the magnetosphere and/or changes due to external conditions. Moreover, our model captures very well the observed local time asymmetry in B_N (weak on the dawnside and strong on the duskside), indicative of the different thicknesses of the current sheet between dawn and dusk that have been identified previously (e.g., Khurana & Schwarzl, 2005; Kivelson & Khurana, 2002).

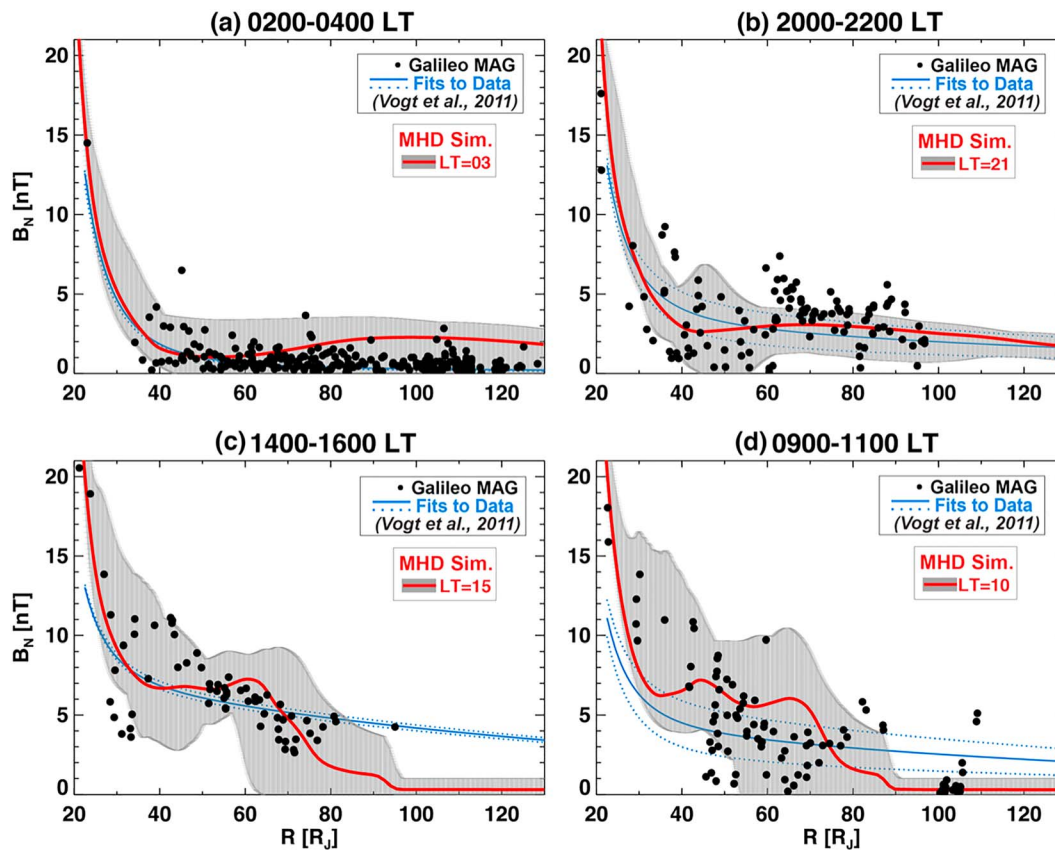


Figure 5. In each panel, the black dots show observations of the magnetic field component (B_N) normal to the current sheet, and the blue solid and dashed lines show fits to the data (adapted from Vogt et al., 2011). The red line in each panel represents the average radial profile of B_N output from our magnetohydrodynamic (MHD) simulation in the same local time sector as the data were collected, and the grey bars in the background show the range of values seen at different simulation times in our global model.

4. Response of the Magnetosphere to Variations of the Upstream Conditions

After creating the quasi-steady state magnetosphere using a purely southward IMF, we continue the simulation in time-accurate mode and perform four simulation runs using the following sets of upstream input:

- Run 1: No change—continued run with fixed southward B_Z and steady solar wind
- Run 2: Introduce a dynamic pressure enhancement (forward shock) under southward IMF
- Run 3: Turn the IMF from a purely southward (B_Z) to Parker-spiral like ($B_Y > 0$).
- Run 4: Introduce a dynamic pressure enhancement (forward shock) under Parker spiral IMF

Two configurations of the magnetosphere were first created: Run 1 for a closed magnetosphere a parallel/southward IMF and Run 3 for an open magnetosphere with a Parker spiral IMF. After the completion of Runs 1 and 3, upstream solar wind conditions were changed to simulate a dynamic pressure enhancement similar to that expected for an interplanetary forward shock (Runs 2 and 4). Solar wind plasma properties and magnetic field magnitude between Runs 1 and 3 were kept the same, that is, same mass density, velocity, and thus dynamic pressure. Likewise, the plasma properties and magnetic field magnitude of the shocked solar wind in Runs 2 and 4 were kept the same, with the only difference being the IMF clock angle. We designed these simulations specifically for understanding the influence of the solar wind dynamic pressure enhancement on Jupiter's magnetosphere under two different states: a closed magnetosphere with minimal impact from dayside reconnection and an open magnetosphere with dayside reconnection expected between the Parker spiral like IMF and the magnetospheric field.

In Figure 6 we show the response of the magnetosphere from these four runs. Plotted in the left and right columns are contours of plasma mass density (log scale) in the meridional plane and equatorial plane,

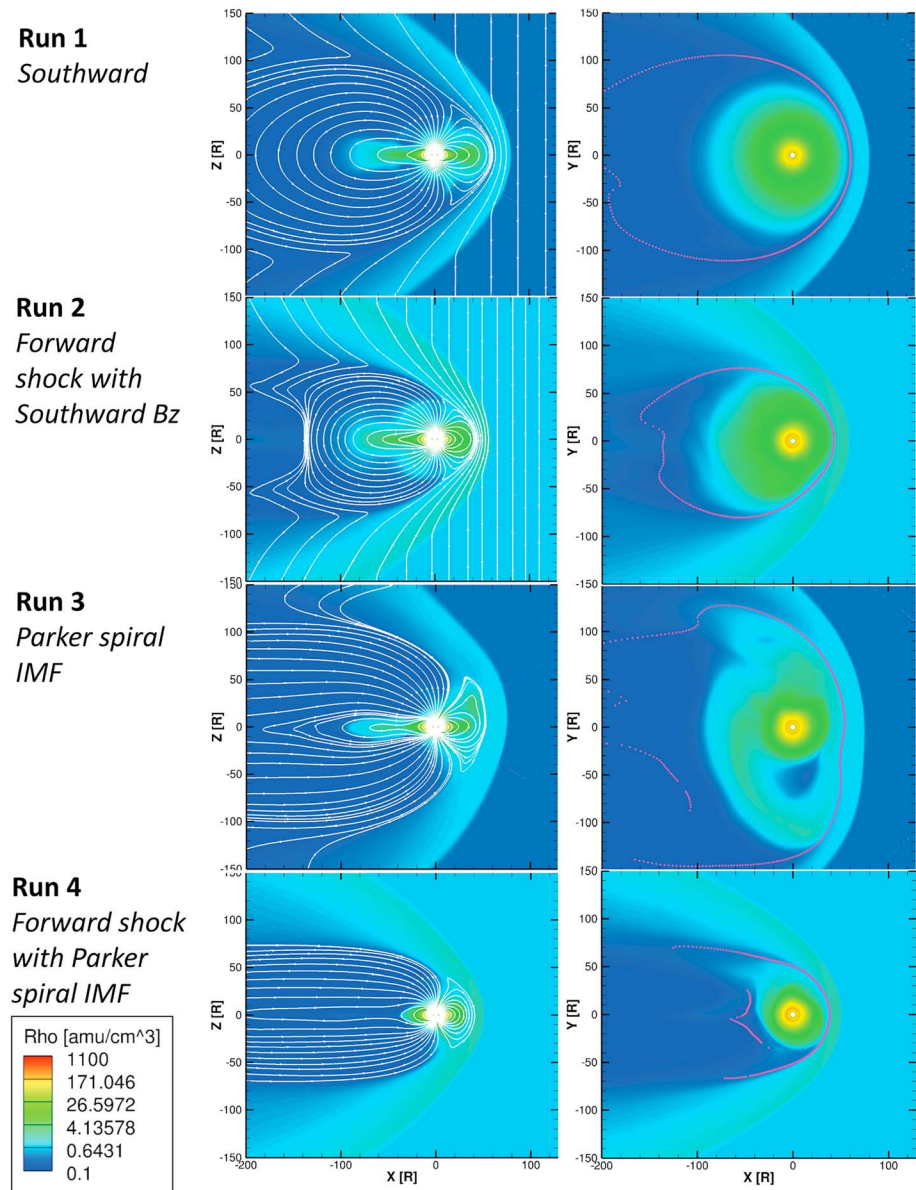


Figure 6. The magnetospheric response to each of the solar wind conditions tabulated in Table 1 at a representative instance in time. The left column shows plasma density contours and projections of magnetic field lines in the meridional plane, whereas the right column shows plasma density contours in the equatorial plane and the equatorial footprints of the last closed field lines (in magenta). IMF = interplanetary magnetic field.

respectively, along with the equatorial footprints of the last closed field lines in a similar format as used for Figure 3. In the meridional ($Y = 0$) plane, we also superimpose magnetic field lines in white that illustrate the disk-like configuration in the inner and middle magnetosphere, which is indicative of the presence of a strong current sheet and departure of the magnetospheric field from dipolar configuration, which is qualitatively consistent with in situ magnetic field measurements (e.g., Khurana, 2001).

4.1. Magnetospheric Response to IMF Rotation (Run 3: From Southward B_z to Spiral IMF With $B_y > 0$)

When the IMF is turned from parallel to a spiral configuration, the magnetic shear across the dayside magnetopause increases such that magnetic reconnection occurs at the dayside magnetopause in the simulation resulting in the twisted dayside magnetic field lines as shown Figure 6, row 3. On the nightside, the

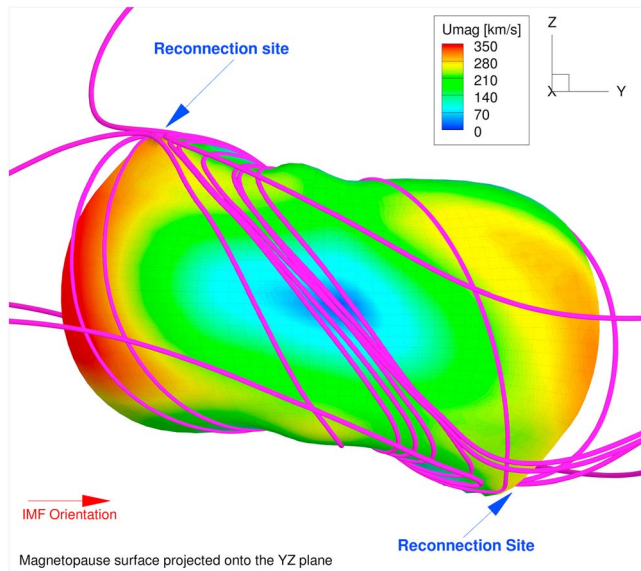


Figure 7. The 3-D magnetopause surface extracted from our model (Run #4) by identifying the separatrix between closed and open field lines on the dayside (06–18 LT), projected onto the YZ plane. The surface is colored by the plasma flow speed. Also plotted are 3-D magnetic field lines, which are colored magenta. Reversal of B_ϕ , highly kinked field lines are observed at high latitudes—in the northern hemisphere on the dawnside (in the $-Y$ direction) and in the southern hemisphere on the duskside (in the $+Y$ direction). The 3-D surface shown spans $[-50, 50] R_J$ in the Y direction, $[-35, 35] R_J$ in the Z direction and $[0, 40] R_J$ in the X direction. The time corresponding to this image is 390 hr, by which time the magnetosphere and the open-closed boundary has reached a quasi-steady state. IMF = interplanetary magnetic field.

equatorial footprints of the last closed field lines provide a good proxy for the reconnection X-line, and we find that after turning the IMF to the Parker-spiral configuration, the tail X-line moves planetward. The tail X-line location also exhibits a dawn-dusk asymmetry, being located further from the planet on the duskside and closer to the planet on the dawnside, consistent with that inferred from observations (Vogt et al., 2010, 2014; Woch et al., 2002). In addition to the planetward shift of the tail X-line, turning the IMF also adds open magnetic flux to the magnetotail lobes, which can also be seen in later plots (Figure 6) where we show the open flux in the ionosphere, and the consequence of the addition of open field lines will be discussed in later sections. As open field lines are added to the tail lobes, the tail magnetic field becomes more stretched with a strong B_x component, in contrast to the dipolar configuration under parallel IMF conditions (Run 1 as shown in row 1 of Figure 6).

4.2. Magnetospheric Response to Dynamic Pressure Enhancement (Runs 2 and 4)

The forward shock introduced in Runs 2 and 4 corresponds to a dynamic pressure enhancement of a factor of ~ 5 (from 0.053 to 0.258 nPa) with the plasma properties upstream and downstream of the shock taken such that the Rankine-Hugoniot shock relations are satisfied. For Run 2 where the IMF is maintained in the parallel orientation that results in a closed magnetosphere, compression by the introduced forward shock causes the bow shock to move from ~ 80 to $\sim 60 R_J$ at the subsolar point, whereas the subsolar magnetopause moves from ~ 60 to $\sim 40 R_J$. In the case of an open magnetosphere (Run 4 where the IMF is in the spiral configuration), the bow shock moves from ~ 75 to $\sim 50 R_J$, whereas the magnetopause moves planetward from ~ 50 to $\sim 40 R_J$ at the subsolar point in response to the shock of the same magnitude as in Run 2. The compression due to the forward shock shrinks the magnetosphere in all directions, including the lobes

and magnetospheric flanks. In both cases of the closed and open magnetosphere, the last closed field lines move planetward on the nightside. Run 4 shows the location of the X-line for the shocked Parker-spiral IMF, and it lies between 50 and $70 R_J$ near midnight. Near the magnetopause flanks, the last closed field lines lie at a distance of $\sim 100 R_J$ from the planet. This creates a peculiar configuration of the magnetotail where the closed field lines extend to larger distances on the flanks than in the midnight sector, similar to that predicted for Saturn by Jia, Hansen, et al. (2012).

For the Parker-spiral IMF configuration used in our simulation, reconnection is found to occur primarily on the magnetopause at relatively high latitudes (at $\sim 50^\circ$ latitude) where the strongest magnetic shear is present. Figure 7 shows a snapshot of the simulated magnetopause surface extracted from Run #4. The magnetopause surface is determined by identifying the separatrix between magnetospheric and magnetosheath field lines based on 3-D field line tracing. The color contours on the magnetopause surface represent plasma flow speeds, and sample field lines are superimposed to show the magnetic topology. As shown, under the spiral IMF configuration with positive B_y , we find that reconnection takes place mainly in two quadrants in the YZ plane: in the northern hemisphere on the dawnside and in the southern hemisphere on the duskside. The reconnection geometry is consistent with the prediction by the analytical model of Masters (2017) for the same IMF configuration.

5. Response of the Ionosphere to Variations of the Upstream Conditions

Figure 8 shows the response of the ionosphere to changes in the different upstream conditions. The left column presents snapshots from each run showing the contours of the current density parallel to the magnetic field (J_{\parallel}). For the northern hemisphere shown here, positive values indicate outward currents and negative values indicate inward currents. The main feature of the current distribution is the circumpolar ring of outward currents centered at $\sim 75^\circ$ latitude. Inside of (or poleward of) the ring are downward

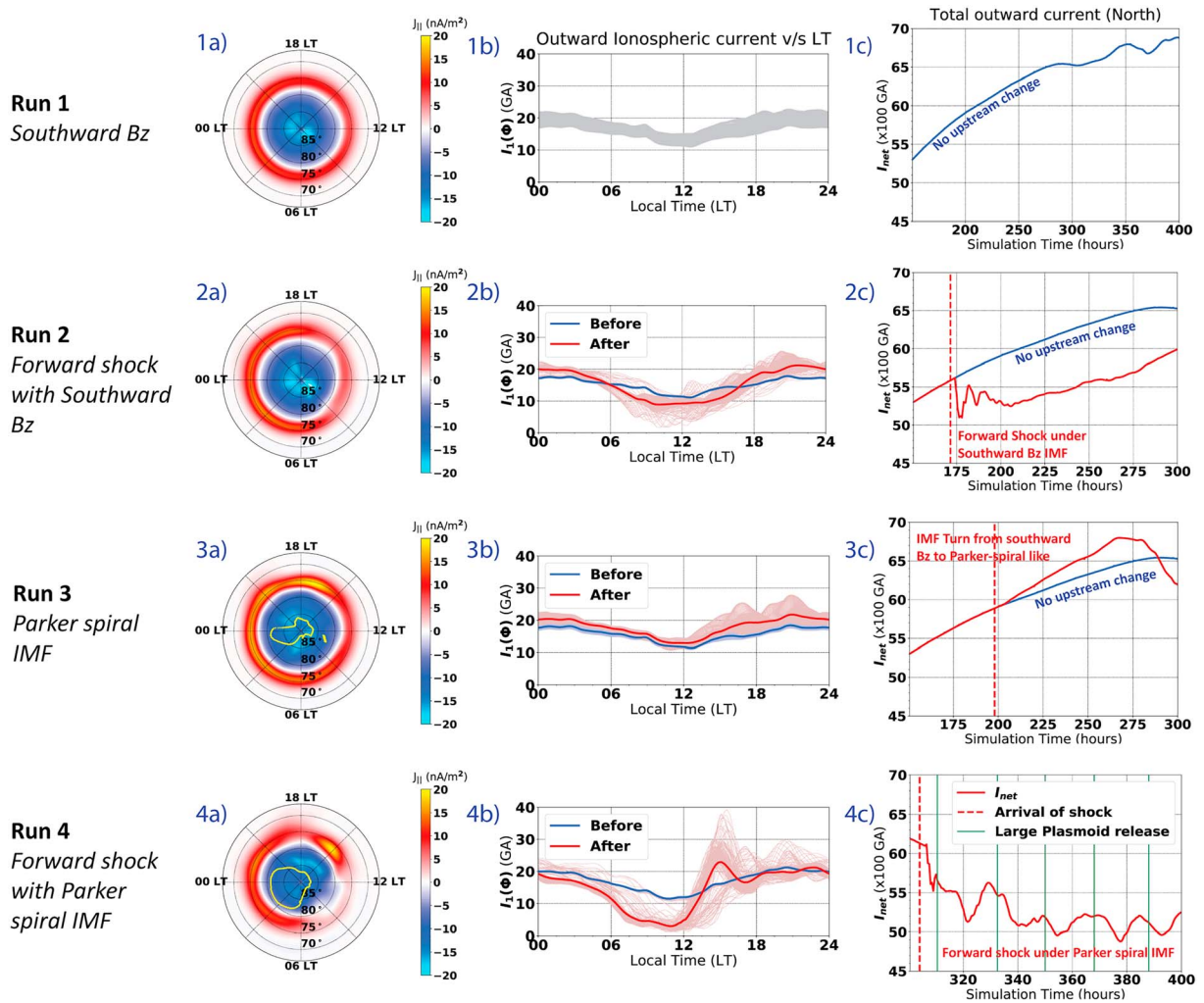


Figure 8. Ionospheric response. Each row represents the ionospheric response to the four runs outlined in Table 1. The first column shows contours of radial current density at the ionosphere with positive values representing outward current. Yellow points are the extracted footprints at the open-closed field line boundaries. In column 2 we show the latitude integrated outward current in the ionosphere as a function of local time. Each curve represents an instance in our simulation, with blue lines representing times before the upstream perturbation reaches the bow shock and red lines representing times after. In column 3 we show the total integrated outward current for all latitudes and local times as a function of simulation time. The blue curves in column 3 represent the variation of total outward current as a function of time for the closed magnetosphere under steady upstream conditions. The red curves represent the same quantity for the particular test case. IMF = interplanetary magnetic field.

field-aligned currents. The upward and downward currents are connected through the horizontal Pedersen currents in the ionosphere, and these currents together make up the corotation enforcement current system.

Note that Ohm's law solver used in our model uses a spherical grid discretized at specific intervals in latitude and local time where each point can be identified by the indices j and i respectively. For a given simulation time n , we first calculate the net outward current (units of amperes) for a particular local time bin i as

$$I_1^n(\phi)_i \approx \sum_{j=1}^{N_\theta} \left(\frac{j_R + |j_L|}{2} \right)_{ij} \Delta S_{i,j}$$

In this equation $j_{R,j}$ is the radial current density at location (i, j) and $\Delta S_{i,j}$ is the area of the spherical rectangle formed by the points $(i + 1/2, j)$, $(i - 1/2, j)$, $(i, j + 1/2)$ and $(i, j - 1/2)$. This parameter I_1 is plotted as a function of local time in column 2 of Figure 8. Each thin line represents the n th time of the simulation with a spacing of 0.5 hr.

Thick blue or red lines represent the average value of I_1 at a particular local time before and after changing the upstream conditions, respectively. As can be seen in column 2, the parameter I_1 is useful for revealing the local time-dependent response of the outward currents, which are thought to be related to the emission intensity of Jupiter's main auroral oval. We then sum I_1 over all local times to obtain the net outward current (units of amperes) in one hemisphere at a particular time n as

$$I_{\text{net}}^n = \sum_{i=1}^{N_\phi} I_1^n(\phi)_i$$

Here N_ϕ and N_θ are the number of grid cells in the azimuthal and meridional directions, respectively. In our simulations $N_\phi = 361$ and $N_\theta = 181$ for each hemisphere. The quantity I_{net} represents the net outward current from one hemisphere and is plotted as a function of simulation time in Figure 8, column 3. The red vertical dashed line represents the time when the upstream perturbation reaches the subsolar bow shock. Blue curves in column 3 represent the trend expected if there was no change in upstream conditions (same the blue curve in Figure 8-1c).

5.1. Ionospheric Response—Run 1 (Fixed Upstream Conditions With Parallel IMF)

For the ~400-hr duration of Run 1 (Figures 8-1a to 8-1c), the magnetosphere remains largely closed due to the southward B_Z IMF imposed at the upstream boundary. Figure 8-1b shows that there is a persistent day-night asymmetry present in the field-aligned current distribution with outward currents stronger on the nightside than on the dayside. Figure 8-1c also shows that the net outward current is steadily increasing with time (and at all local times/longitudes), despite the upstream conditions being constant. Initially, the rate of increase of the currents is almost linear, but with time the growth rate decreases and eventually the currents are seen to decrease. We believe that the growing trend of currents (with time scales of tens of hours), in the absence of any change in external conditions, is due to internal factors. As the magnetosphere builds more mass due to mass loading in the Io plasma torus, more torque is required from the ionosphere in order to force the magnetospheric plasma to corotate with the planet. Alternatively, consistent mass loading would increase the bend back of the magnetic field lines, which would increase magnetic field strength in the high-latitude regions thereby increasing $J_{||}$ in the ionosphere. Hence, prolonged mass loading in the absence of mass loss mechanisms, such as plasmoid release, would require an increase in the corotation enforcement currents. Indeed, we see that the ionospheric currents decrease only when a plasmoid is released (at around $t = 350$ hr), suggesting that with the release of mass to the magnetotail, the net strength of the corotation enforcement circuit is reduced. For comparisons with other runs, the curve showing the expected trend of the total current (i.e., Figure 8-1c) is included in all subfigures in the last column.

5.2. Ionospheric Response—Run 3 (Turning of the IMF to $B_Y > 0$)

In Run 3, the upstream plasma properties are kept the same as in Run 1, and a tangential discontinuity is introduced in the solar wind across which the IMF is rotated from southward to the Parker-spiral configuration (with $B_Y > 0$). As shown in Figure 8-3a, reconnection at the magnetopause produces open magnetic field lines, and the open-closed field line boundary (OCB; marked in yellow lines) starts to expand equatorward. At the time shown in this plot, which is roughly 75 hr after the IMF turning, the region of open field lines extends about a few degrees from the pole and the OCB lies at least 5° poleward of the main oval of outward currents. Similar to that in Run 1 (Figure 8-1b), the outward currents in this run (Run 3) are stronger on the nightside than on the dayside (Figure 8-3b) and a continuously increasing trend is seen for the net outward current (Figure 8-3c). The red dashed line in Figure 8-3c marks the time when the discontinuity reaches the subsolar bow shock, and we can see that the rate of increase of currents (shown by the red line) deviates from the curve expected if there were no change in the upstream conditions (shown in blue). Note that the only upstream change introduced in this run is the change in IMF clock angle. Therefore, the comparison between Run 1 and Run 3 indicates that a change in IMF orientation can have significant influences on the large-scale current systems. The increasing trend of current, which now has a larger slope, eventually changes to a decreasing trend after the release of a plasmoid at $\sim t = 270$ hr, consistent with the behavior seen in Run 1.

5.3. Ionospheric Response—Runs 2 and 4 (Dynamic Pressure Enhancement)

In comparison to an IMF rotation, the response of the ionosphere to a forward shock, that is, a dynamic pressure enhancement, in the solar wind is more dramatic. In Runs 2 and 4, we have introduced a dynamic pressure enhancement (a factor of 5 larger than the background). First, we examine Run 2—that is, dynamic pressure enhancement under a closed magnetosphere (Figures 8-2a–2c). In all our simulation runs, we find the nightside currents to be stronger than the dayside, and it can be seen from Figure 8-2b that the introduction of a forward shock makes this asymmetry more pronounced; that is, the nightside currents get stronger whereas the dayside currents get weaker. Similar enhancement of the day-night asymmetry has also been seen in the MHD model of Chané et al. (2017). Apart from the overall response, there are also noticeable local time-dependent responses: Transient peaks in the outward current appear at specific local times. Our simulation predicts a minor enhancement on the nightside (10–20% increase in total currents) and a large decrease in current on the dayside (between 10% and 60%). As a result, the net outward current (I_{net}) sharply decreases after the impingement of the shock. After ~50 hr, the system recovers and an increasing trend of the net outward current is seen again.

Our findings are consistent with previously published theoretical models (Cowley & Bunce, 2003; Cowley & Nichols, 2007; Southwood & Kivelson, 2001), which have predicted that a dynamic pressure enhancement, and subsequent compression of the magnetosphere, would lead to an increase in azimuthal velocity of the plasma as it conserves angular momentum. In theory, this should decrease the strength of the corotation enforcement current system on the dayside. Consistent with this prediction, we find an increase in angular velocity inside the magnetosphere on the dayside after the shock compression, which leads to much reduced outward field-aligned currents in the dayside ionosphere.

A similar behavior was also found for Run 4—that is, dynamic pressure enhancement with a Parker spiral IMF (Figures 8-4a to 8-4c). Due to the increase of magnetic flux reconnecting on the dayside and the release of plasmoids on the nightside (which serves to close previously opened tail lobes), we find a prominent region of open field lines in the polar region. We also find a very strong response of the ionospheric currents, with dayside currents drastically decreasing in strength (by 50–60%), whereas the nightside currents appear almost unaffected (Figure 8-4b). Consequently, the net outward current also decreases sharply after the dynamic pressure enhancement at $t = 310$ hr. A key difference between Figure 8-4c and Figures 8-1c, 8-2c, and 8-3c is that the time history of the total outward current did not recover back to the increasing trend after the dynamic pressure enhancement. This may be due to very frequent plasmoid releases in the magnetosphere after the shock compression. As seen in Runs 1 and 3, a decrease in the net outward current is well correlated with times at which a plasmoid is released. It is also noteworthy that the response of the ionosphere to the forward shock was stronger in Run 4 (open magnetosphere) than in Run 2 (closed magnetosphere). Apart from the IMF orientation, there is another difference between Runs 2 and 4: the phase of the magnetosphere in the Vasyliunas cycle. While Run 4 was started ~30 hr after the release of a large plasmoid, Run 2 was initiated at a time when the magnetosphere was still in the process of accumulating mass with no prior plasmoid release. It is possible that the differences in the strength of the response may be due in part to the differences in the internal state of the magnetosphere, that is, depleted versus filled magnetosphere, rather than just the orientation of the external IMF. Clearly more work is needed to conclusively separate the internal and external influences.

6. Plasmoid Release and Variation of Open Magnetic Flux

In all simulations listed in Table 1, tail reconnection occurs and produces plasmoids. For instance, a large plasmoid can be seen in Figure 6, row 3 in the form of a high-density region between 00 and 06 LT. After initially being created at a radial distance of ~50–70 R_J on the dawnside, the plasmoid is seen to grow and move tailward, eventually escaping the magnetosphere and lost to the solar wind. In Run 4, a vortex structure is created in the magnetosphere on the duskside at around 40 R_J radial distance from the planet (not shown). The vortex is formed subsequent to a large reconnection event in the magnetotail and it strengthens as it moves sunward, eventually reaching the postnoon sector. The vortex is made of corotating and anticorotating flows and produces a strong ionospheric response in the postnoon sector (Figures 8-4a and 8-4b near 16 LT). We believe that this vortex and the subsequent localized bright spot in J_{\parallel} observed near 16 LT in the ionosphere are due to the interaction of return flow from the duskward tail reconnection site with the

corotating magnetospheric plasma and has also previously been observed by Fukazawa et al. (2006) using their MHD model.

In Figures 8-3a and 8-4a the yellow points superimposed onto the contour plots correspond to the OCB identified in our simulations. For each local time and longitudinal position in the ionosphere, we trace 3-D magnetic field lines from a sphere at $3 R_J$ to identify any transition between open and closed field lines. If a transition is found, its location on a $1 R_J$ sphere is determined by using a dipole field line trace, which is then plotted in Figure 9. Even with 1° resolution in both latitude and longitude, our tracing algorithm does not find any such transition during times when the IMF is southward, which is consistent with the picture that the magnetosphere is largely closed under such external conditions. In contrast, under a Parker spiral IMF, the OCB increases in size with time and can reach a latitude of $\sim 80^\circ$ on the nightside under strong solar wind driving (column 4). While the size of the OCB tends to vary depending on the upstream conditions, for the various upstream conditions examined in our simulations it is always located poleward (by at least a few degrees) of the main oval of upward field-aligned currents arising from corotation breakdown, which lies at $\sim 75^\circ$ latitude.

For further analysis we divide the magnetic field lines extracted from our MHD model into four categories, denoted by the “status” variable (Table 2). A status value of 0 represents a closed field line with both ends connected to the planet. A status value of 1 or 2 implies an open field line with one footprint in the northern or southern hemisphere, respectively, while a status value of 3 refers to those field lines with both ends in the solar wind, which we call disconnected field lines. Figure 9 shows the status of field lines seeded from the northern and southern ionosphere, whereas Figure 11 shows the status of field lines seeded from the equatorial plane in the magnetosphere.

6.1. Magnetic Topology Associated With Plasmoid Release

In Figure 9, we show the status maps of the northern and southern hemispheres on a $1 R_J$ sphere, at different times during the sequence of a plasmoid release. For both hemispheres, the cyan regions contain field lines that are closed (status = 0). For the northern hemisphere panels, the dark blue regions contain open field lines (status = 1) that magnetically map to the solar wind. For the southern hemisphere panels, the red regions indicate open field lines (status = 2) that map to the solar wind. It is immediately clear from Figure 9 that these status maps are not north-south symmetric, with stark differences in the topology between the two hemispheres.

Two plasmoids are observed in the magnetosphere during the times shown in Figure 9: a relatively small size plasmoid on the duskside and a much larger plasmoid near dawn. When the plasmoids are initially formed, they contain predominantly closed flux. This is consistent with the idea that plasmoids form due to the Vasyliunas cycle are created on closed field lines. As the plasmoids move tailward, they grow in size and create a region of closed flux inside the polar cap. The large plasmoid in the dawn sector of the magnetosphere can be identified by its status signature on the dawnside in the form of a large region of closed flux, whereas the smaller plasmoid in the dusk sector also creates a similar region of closed flux in the duskward polar cap. With time, the plasmoids grow and interact with the surrounding plasma and magnetic field, which creates rather complicated magnetic field structures that contain intertwined open and closed field lines (Figure 9b). As the plasmoids move further down the magnetotail, they grow in size and the status signatures associated with plasmoids move toward midnight (previously at dawn and dusk) and the high-latitude region in the ionosphere starts to be filled with open field lines. With time, the ratio of open field lines to closed field lines in the plasmoid footprint increases in both the northern and southern hemispheres. As a result, the tail plasmoids, when mapped magnetically to the ionosphere, correspond to a stripe-like structure.

Observations of the polar aurorae of Jupiter show various intriguing features such as arcs and filaments (e.g., Grodent et al., 2003; McComas et al., 2007; Nichols et al., 2009) that have been suggested to be linked to dynamic processes in the solar wind and magnetotail. Our simulation results show that the polar regions of the planet, which are often assumed to lie on open field lines, may magnetically connect to distant regions in the magnetotail associated with a plasmoid. While our MHD simulation does not directly model the kinetic physics of particle energization associated with reconnection, the magnetic topology associated with plasmoid release and propagation through the tail region as seen in our simulation suggests that

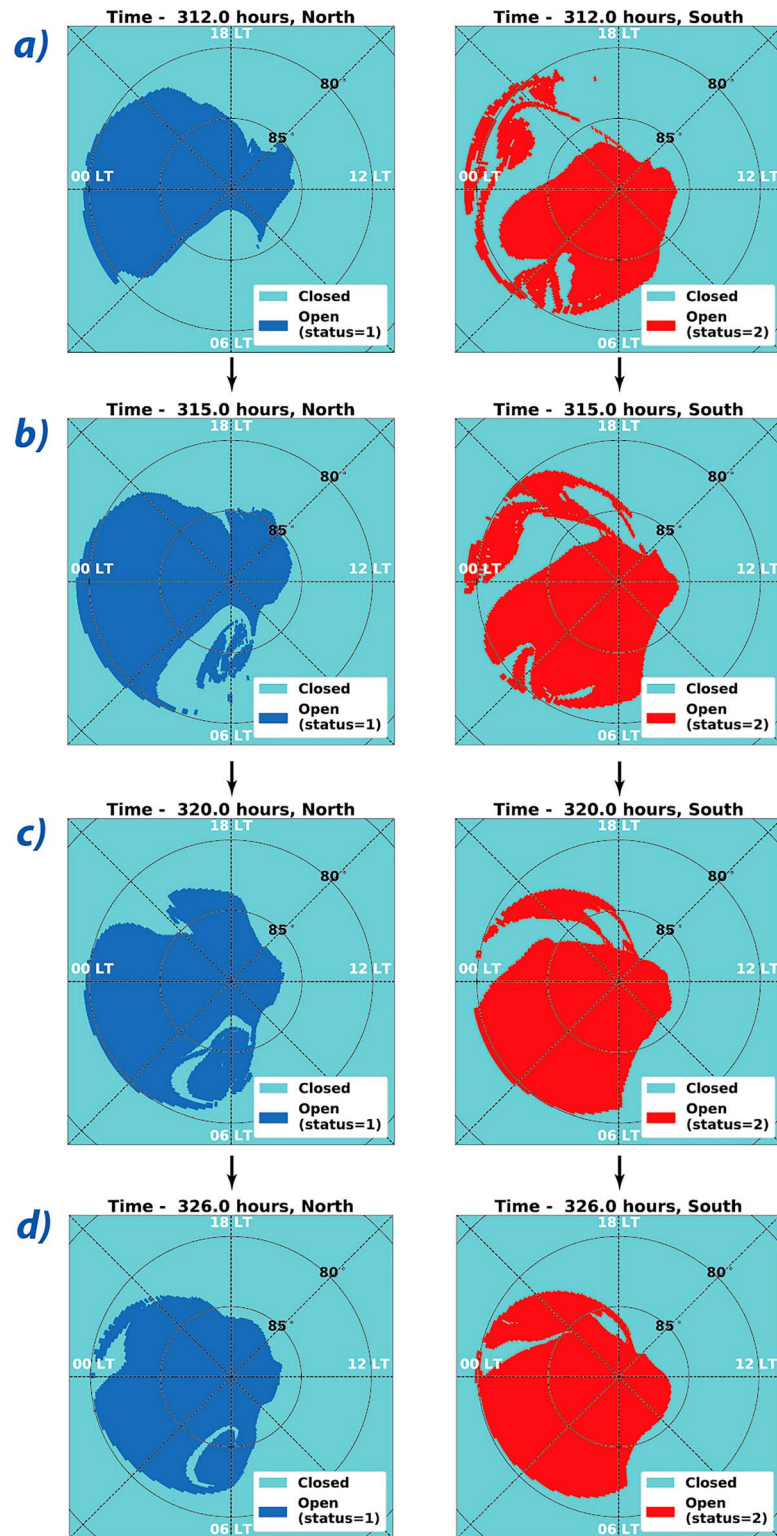


Figure 9. (a–d) Ionospheric maps showing regions of open and closed field lines at different times of the simulation under a Parker-spiral interplanetary magnetic field with comparatively high solar wind dynamic pressure. Red and dark blue shaded areas represent regions of open magnetic field lines, while the pale blue regions contain closed field lines. The footprint of the plasmoid can be identified as a region of initially closed flux on the dawn sector, which slowly fills up with more open flux. Also note the differences between the northern and southern hemispheres. The color schemes are the same for this figure and Figure 11.

Table 2
Definition of the “Status” Variable and the Color Scheme Followed in Figures 9 and 11

Status variable value	Description	ID	Color code
0	Closed field line	Closed	Cyan
1	Open field line with one footprint in the northern hemisphere of Jupiter	Open type N	Dark blue
2	Open field line with one footprint in the southern hemisphere of Jupiter	Open type S	Dark red
3	Open field line with both footprints in the solar wind	Disconnected	Yellow

energization associated with tail plasmoid release may provide a plausible explanation for the observed arc-like or filament-like aurora structures.

In Figure 10, we show the three-dimensional magnetic field lines associated with the tail plasmoid along with the plasma density contours in the equatorial plane. Orange field lines are closed field lines, whereas black field lines are “disconnected” field lines with both ends in the solar wind. It can be seen that although the plasmoid is generated on and still contains closed field lines, it is surrounded by open field lines as it moves tailward. The inset in Figure 10 shows the corresponding ionospheric status map in a similar format as Figure 9. Since this plasmoid is noticeably smaller, it has a smaller, but consistent, status signature in the form of a region of closed flux in the polar cap on the nightside.

6.2. Open Flux in the Magnetosphere

To complement the analysis of the status of field lines shown in section 6.1, we repeated the same procedure of tracing field lines starting in the equatorial plane of the magnetosphere. The corresponding magnetospheric status maps are shown in Figure 11 for two different types of plasmoids that we will call Type 1 and Type 2, respectively. The left column shows a plasmoid of Type 1, which is a large plasmoid released on the dawnside, whereas the right column shows a plasmoid of Type 2, which is released near midnight. Both plasmoids have some common features, namely, they both originate from closed field lines. After release, the Type 1 plasmoid severely distorts the magnetic topology of the magnetotail. Upon close examination, one can see regions of closed field lines interspersed within large regions of open field lines. The Type 2 plasmoid, on the other hand, has a cleaner topological fallout. After being detached as a “blob” of closed flux, the Type 2 plasmoid is surrounded by disconnected field lines (status = 3, both ends in the solar wind)

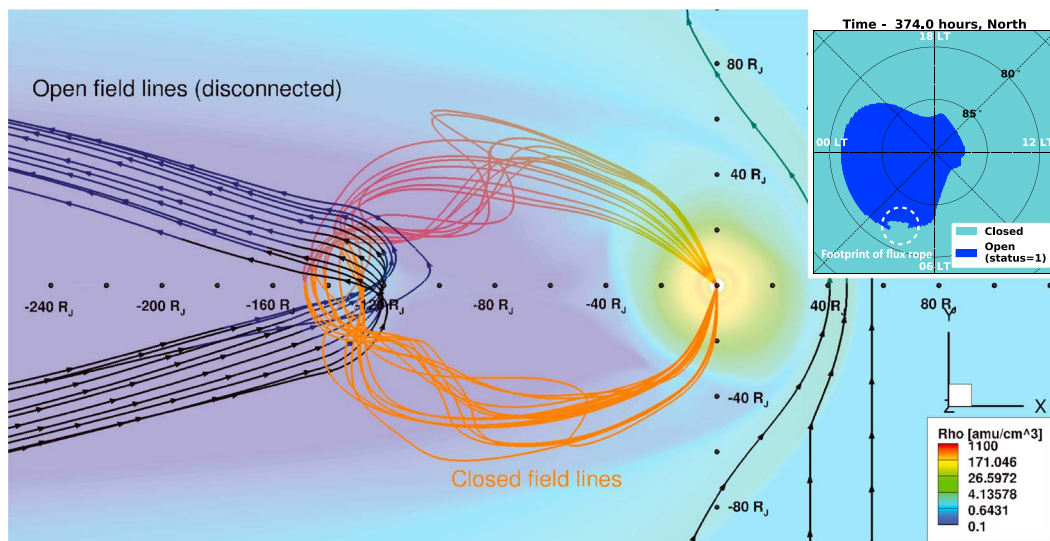


Figure 10. Contours of plasma density in the equatorial plane along with superimposed 3-D magnetic field lines. Orange field lines thread a plasmoid in the magnetotail and have both ends connected to the planet (i.e., closed). Black field lines are field lines with both ends in the solar wind, which envelope the flux rope structure. The inset shows the flux map at $1 R_J$ where dark blue regions denote open flux (similar to Figure 8). The plasmoid creates a region of closed flux inside the open polar cap (marked by dashed circle in the inset figure). Note that the 3-D magnetic field lines cross the equatorial plane, so different colors on the same closed field line is a shading effect as the translucent density colors are mixed with the orange color of the field lines in the southern hemisphere.

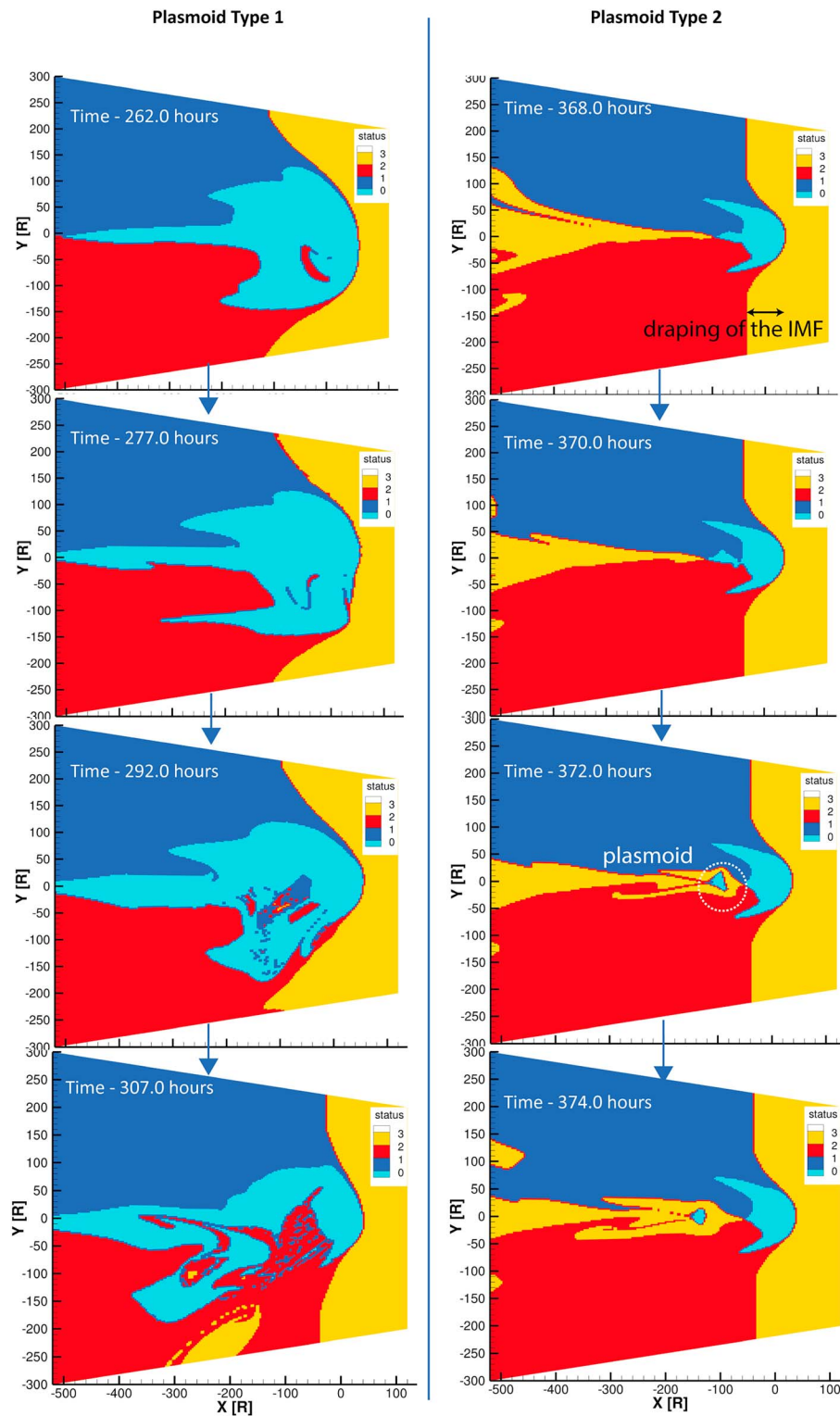


Figure 11. Maps showing the “status” of the field line seeded from the equatorial plane (status 0 = closed [cyan], 1 = Open with one end connected to northern hemisphere [blue], 2 = open with one end connected to the southern hemisphere [red], 3 = Open with both ends in the solar wind/“disconnected” [yellow]) for different times in our simulation. The left and right columns illustrate how different plasmoids change the magnetic topology of the magnetotail. The colors are consistent between this figure and Figure 9. The IMF for all cases presented here lies in the XY plane and points to the +Y direction. The Type 1 plasmoid shown is generated during a period of low upstream dynamic pressure while the Type 2 plasmoid shown here is released during a period of higher upstream dynamic pressure. IMF = interplanetary magnetic field.

even though it is located deep inside the magnetosphere. With time, the Type 2 plasmoid moves tailward and the region of closed flux associated with the plasmoid decreases in size. However, the region of disconnected flux in the magnetotail expands after the release of a Type 2 plasmoid.

Another feature which can be recognized in Figure 11 is the stark separation between dayside disconnected field lines and the open (status = 1 and 2) field lines on the dawn and dusk flanks, as can be identified through the vertical demarcation at $x = -40 R_J$ in column 2. We traced 3-D magnetic field lines which suggest that this vertical demarcation is linked to the draping of the IMF around the magnetopause (we call this distance x_{draping}). That field lines in the magnetosheath drape around the magnetopause has been discussed in detail for Earth and Saturn (Crooker et al., 1985; Sulaiman et al., 2014, 2017) and is expected to be more pronounced at Jupiter due to the large polar flattening of the magnetosphere (Erkaev et al., 1996; Farrugia et al., 1998; Slavin et al., 1985). While our model does predict the draping of the IMF around Jupiter's magnetopause, the degree of polar flattening in our model is lower than previous predictions ($\epsilon = -0.3$, expected to be ~ 0.8 according to Slavin et al., 1985).

6.3. Rate of Change of Open Flux in the Magnetosphere

After identifying the status of each point on the $1-R_J$ sphere for multiple times in our simulations, we integrate the open magnetic flux within the open field region in the northern hemisphere of the planet. Figure 12 a shows the variation of this calculated open flux in our model as a function of simulation time for Parker-spiral IMF (purely B_y) but different solar wind dynamic pressures. The black points show the open flux calculated in our simulation, while the dashed red vertical line marks the time when the introduced forward shock arrives at the bow shock. To reveal potential correlation between plasmoid release and open flux variations, we overlay solid lines in this figure to mark the times when plasmoid release occurs in the simulation. We identify plasmoids in the model based mainly on the B_z component (the normal component to the tail current sheet). A bipolar variation of B_z in the equatorial plane is an indication that a reconnection event has occurred in the magnetotail. Typically, plasmoids generated in our model tend to grow in size as they move tailward. Therefore, we further divide the identified plasmoids into two groups based on their maximum size in the cross-tail direction (y direction): large plasmoids which have a cross-tail width larger than $50 R_J$ at their maximum extent and small plasmoids whose maximum width is $< 50 R_J$. Green thick lines and thin blue lines represent the times when large and small plasmoids are released, respectively.

Prior to the shock arrival at $t = 302$ hr, the IMF along with the solar wind parameters remain fixed. During this interval, the open flux in our model gradually builds up due to the magnetopause reconnection. At around $t = 223$ hr (marked by the solid green vertical line), a relatively large plasmoid with a cross-tail width exceeding $50 R_J$ forms in the magnetotail that closes some of the open flux stored in the tail lobes, which can be seen as the change of slope in the time history of the open flux. During this period, there are also a couple of smaller-scale plasmoids (with cross-tail width $< 50 R_J$) formed, as marked by the solid blue vertical lines in Figure 9. After the shock arrival at $t = 302$ hr, the rate at which the open flux is added to the polar cap increases due to the enhanced solar wind convective electric field associated with the shock. About 25 hr after the shock impact, a large-size plasmoid is formed and released in the tail that results in a significant reduction of the open flux. After the impingement of the shock, the compressed magnetosphere experiences frequent plasmoid release, both large and small. Compared to the situation seen in the simulation during the nominal solar wind conditions where plasmoid release occurs every 20 to 50 hr, the occurrence rate is significantly higher in the compressed case, which is of the order of one plasmoid every few hours. A similar behavior has been seen in the MHD model of Saturn by Jia, Hansen, et al. (2012), who found more frequent plasmoid releases during periods of stronger solar wind driving.

The time variation of the open flux provides a useful measure of how the magnetosphere responds globally to the solar wind driving and internal dynamics. As discussed above, dayside reconnection would add open flux to the polar cap whereas tail reconnection would potentially close open flux stored in the tail lobes. Therefore, the time rate of change of the open flux can be used to quantify the global reconnection efficiency, which depends on the difference in the reconnection rates between the dayside magnetopause reconnection and the tail reconnection. At the beginning of the simulation, in the absence of tail reconnection, we find that the open flux increases at a rate of ~ 284 kV, which corresponds approximately to the global reconnection rate under the solar wind conditions listed in Table 1, column 2.

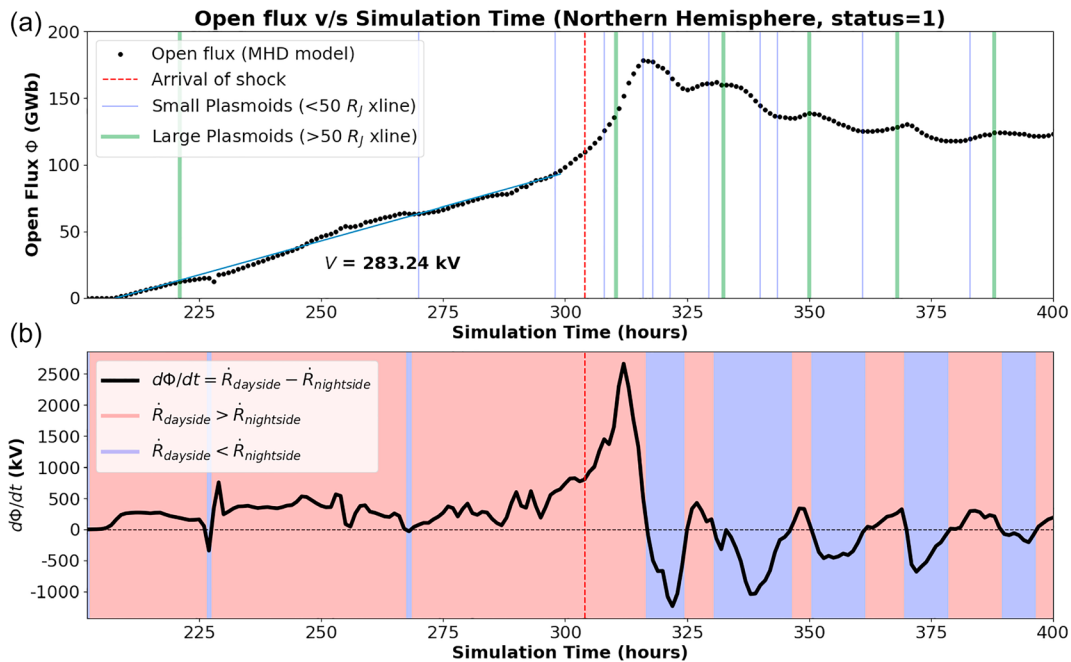


Figure 12. (a) Variation of the total open flux (in the northern hemisphere), Φ , as a function of simulation time. Times at which plasmoids are initiated are marked as vertical lines in the plot. The red dashed vertical line marks the arrival of the shock at the bow shock. Plasmoids that have an X-line size of at least $50 R_J$ when fully developed are represented by thick green lines, whereas smaller plasmoids (X-line length $< 50 R_J$) are shown in thin blue vertical lines. (b) Time rate of change of the total open flux ($d\Phi/dt$) as a function of simulation time. Intervals with positive $d\Phi/dt$ are shaded red, while intervals with negative $d\Phi/dt$ are shaded blue.

In Figure 12b, we show the calculated rate of change of open flux in the northern hemisphere (status = 1), that is, $d\Phi/dt$ as a function of simulation time. After the shock is introduced in the simulation, the rate of increase of open flux increases, corresponding to a peak global reconnection potential of ~ 2 MV. This increase in the reconnection rate on the dayside is primarily due to enhanced solar wind speed and increased IMF strength due to compression and hence the convective electric field behind the shock. At later times, the open flux in our simulation is found to decrease and increase periodically at a period of ~ 20 hr, highlighting the competing influence of magnetopause reconnection (which serves to open magnetic flux) and nightside reconnection (which decreases the net open magnetic flux). Closer examination reveals that the decreases in open flux are also correlated with the release of large plasmoids. Walker and Jia (2016) report on simulations of the Jovian magnetosphere performed by Fukazawa et al. (2010) and also found quasi-periodic increase and decrease in open flux with a similar period of ~ 20 – 30 hr.

In discussing Figure 9 we noted that the release of plasmoids creates a region of open flux in the polar cap, which may seem contradictory to these findings. However, it must also be noted that the overall size of the polar cap also depends on many other factors, such as the difference between reconnection rate on the dayside versus the nightside. Figure 11 clearly demonstrates that plasmoid release increases the amount of disconnected flux in the magnetosphere. Since the disconnected field lines, by definition, cannot magnetically map to the northern hemisphere, they are not accounted for in our calculation for net open flux which is done on a $1 R_J$ sphere for Jupiter (thereby only considering status = 1 type field lines). Figure 11 also shows that with the increase of disconnected flux in the magnetotail, the amount of connected open flux (i.e., status = 1 and 2) decreases. This would decrease the overall size of the polar cap, which would lead to decreased status = 1 flux. The overall shrinking of the polar cap can also be seen in Figure 9.

As time progresses the dayside and nightside reconnection rates seem to approach steady state, which can be seen in Figure 12b where fluctuations in $d\Phi/dt$ decrease with time. For the compressed magnetosphere, at the end of our simulation ($t = 400$ hr) the total open flux amounts to ~ 120 GWb. It is interesting to note that the creation of open flux is largely due to the reconnection on the magnetopause, and the result that the net open flux seems to reach a steady state implies that flux closure on the nightside or elsewhere is happening in

a manner expected by the terrestrial-like Dungey cycle. Although we have not yet identified any preferential spatial location where flux closure is consistently occurring, it is clear that both Vasyliunas cycle reconnection (detachment of plasmoids on closed field lines) and Dungey cycle-type flux closure contribute to the circulation of magnetic flux in Jupiter's magnetosphere.

Plasmoids generated in Jupiter's magnetotail may be a result of a near-planet like flux closure event attributed to the Dungey cycle or a result of centrifugal stresses exerted on the corotating plasma, that is, the Vasyliunas cycle, both of which may cause reconnection onset on closed field lines. When the IMF is southward (Run 1), absence of dayside magnetopause reconnection would essentially shut off the Dungey cycle. However, plasmoids are still observed in this case (not shown), and they are a direct product of the Vasyliunas cycle. In this case the plasmoid, once generated, is constrained by the surrounding closed field lines, and "escapes" through the magnetopause. In contrast, when the IMF is in the Parker-spiral configuration, dayside magnetopause reconnection would add open flux to the tail lobes. In this scenario, plasmoids generated due to a tail reconnection event may induce closure of open flux in the tail lobes (Cowley et al., 2008) regardless of the original cause of reconnection onset. The lobe reconnection-produced field lines, which are carried by fast-moving reconnection jets moving behind the plasmoids, would facilitate the escape of plasmoids down tail. These findings from our Jupiter simulations are similar to those reported for global simulations of Saturn's magnetosphere (Jia, Hansen, et al., 2012).

As noted earlier, the global simulation presented here is based on an ideal MHD model, in which no kinetic physics is included to describe reconnection. However, reconnection does occur in MHD simulations, which is facilitated by numerical resistivity. It is interesting to compare the global reconnection rate and the resultant amount of open flux in our MHD model with prior estimates based on observations and analytical models. For instance, Masters (2017) presented an analytical method to estimate the total reconnection potential at Jupiter's magnetopause under different solar wind conditions, and he predicted a dayside reconnection potential ranging between 200 and 1,000 kV. The reconnection potentials estimated in our simulations are in general agreement with the Masters model results. Further, based on auroral observations and magnetic field modeling, Nichols et al. (2006) and Vogt et al. (2011) estimated the typical amount of open flux present in Jupiter's magnetosphere, and their results give a range of 300–700 GWb. The maximum amount of open flux seen in our simulations is about 175 GWb, which is slightly lower than previous estimates and could be related to our use of an ideal axisymmetric dipole for the planetary magnetic field.

7. Summary and Conclusions

We have developed a new MHD model for Jupiter's magnetosphere using the BATSRUS MHD code. Time-dependent simulations have been conducted with various upstream conditions to investigate how Jupiter's magnetosphere responds to changes in the solar wind and IMF properties. As model validation, we compare the modeled density, velocity, thermal pressure, magnetic field, and plasma β extracted from multiple time steps and from simulation runs with different external conditions with available in situ observations and found generally good agreements. In particular, while our model underpredicts the plasma density (and pressure) in the inner magnetosphere ($<10 R_J$) due to potential reasons of grid resolution and/or the assumption of isotropic pressure in ideal MHD, our model results match very well the statistical results from observations outside of $10 R_J$ in terms of plasma density, azimuthal velocity, and the magnetic field. Further, our model also captures the dawn-dusk asymmetries in the thickness of the current sheet (e.g., Khurana & Schwarzl, 2005; Vogt et al., 2011) as observed by the Galileo spacecraft, that is, thicker current sheet on the duskside compared to dawn. The locations of the magnetopause and bow shock in our model are also generally consistent with the predictions by the empirical models of Joy et al. (2002), although our simulated magnetopause is slightly smaller in size due to the lack of energetic particles in the MHD model.

After creating a quasi-steady state magnetosphere in the simulation, we introduce various types of changes in the upstream solar wind and IMF, such as an IMF rotation and a dynamic pressure enhancement under southward IMF and Parker spiral IMF conditions. We find that changing the IMF orientation from a southward (parallel) to Parker-spiral like IMF creates open flux in the magnetosphere and thereby modifies the large-scale magnetospheric configuration, but it alone has little effect on the corotation enforcement current system. However, in the cases where a forward shock is introduced in the solar wind, it has a significant impact on the global magnetosphere-ionosphere system. In particular, all of our simulations show that

there is an apparent asymmetry in the field-aligned current intensity in the ionosphere between the dayside and the nightside, with more intense currents on the nightside. This day-night asymmetry is further enhanced by the compression of the magnetosphere by a forward shock. In the simulation where a shock is introduced under Parker-spiral IMF conditions (Run 4), a region of intense field-aligned currents is present in the afternoon local time sector (16 LT; Figures 8-4a and 8-4b), which magnetically maps to a region in the middle magnetosphere containing vortical plasma flows created due to the interaction between the return flow from tail reconnection with the corotating plasma. Although the ionospheric currents respond to the forward shock in both simulations (Runs 2 and 4), the magnitude of the response is significantly different. In general, when the magnetosphere contains more open flux (Run 4) due to dayside reconnection, the response of the ionosphere is stronger. It should be noted that while these two runs use the same solar wind parameters with the only difference being the IMF orientation used, the magnetospheric states prior to the shock impact are quite different, which may contribute in part to the differences seen in the simulated response. Future work is needed in order to isolate these two effects, that is, preconditioning of the magnetosphere and the influence of the IMF orientation.

Plasmoid release in the tail has long been suggested to be an important means of plasma transport, and signatures of plasmoids have indeed been found in various in situ observations in Jupiter's magnetotail. Our global simulations also show plasmoid formation and release due to reconnection in the magnetotail. The majority of plasmoids seen in our simulations appear to form initially on closed magnetic field lines, consistent with the picture proposed by Vasyliunas (1983). While differing in size, all the plasmoids produced in the simulations develop a complex magnetic topology as they evolve and propagate downtail. As an example, we have shown the time evolution of two plasmoids with different sizes and their mapping to the polar ionosphere. Our magnetic mapping results support the previous hypothesis that the complex morphology of tail plasmoids may be responsible for creating puzzling auroral features such as arcs and filaments (e.g., Grodent et al., 2003; McComas et al., 2007; Nichols et al., 2009).

As a quantitative measure of the influence of the external driver on the global magnetospheric configuration, we have identified the OCB throughout our simulations by tracing 3-D magnetic field lines. We have also calculated the total amount of open flux within the magnetosphere and examine the time evolution of the open flux in response to the changes imposed on the upstream parameters. For southward IMF, the magnetosphere has little to no open flux, as expected. As the IMF orientation is changed to a more realistic Parker spiral configuration, open magnetic flux starts to be added to the magnetosphere due to the dayside magnetopause reconnection and as such the OCB in the ionosphere starts to expand in size moving equatorward. In all the simulations present here, the OCB is found to be always located poleward by at least a few degrees of the main oval of upward field-aligned currents associated with corotation breakdown. The total amount of open flux is found to peak around 200 GWb for typical Parker-spiral IMF conditions, which is about a factor of 2 smaller than previously published estimates (e.g., Vogt et al., 2011). There is a clear correlation between the reduction of open flux and the release of plasmoids in the tail, whose occurrence frequency appears to be affected by the solar wind convective electric field with more frequent release under stronger driving. Based on the time rate of change of the open magnetic flux, we estimate the average potential drop associated with the dayside reconnection under nominal solar wind conditions to be approximately 280 kV, which is about a factor of 2 lower than previous estimates (e.g., Masters, 2017).

In the present study we have assumed that Jupiter's internal magnetic field is an axisymmetric dipole. However, recent observations by Juno have revealed significant north-south asymmetries in the internal magnetic field (Connerney et al., 2018) due to the presence of large higher order moments. How the complex internal magnetic field influences the magnetosphere and its interaction with the ionosphere and the solar wind remains an outstanding question that needs to be addressed in future work.

References

- Bagenal, F., & Delamere, P. A. (2011). Flow of mass and energy in the magnetospheres of Jupiter and Saturn. *Journal of Geophysical Research*, 116, A05209. <https://doi.org/10.1029/2010JA016294>
- Blanc, M., Andrews, D. J., Coates, A. J., Hamilton, D. C., Jackman, C. M., Jia, X., et al. (2015). Saturn's plasma sources and associated transport processes. *Space Science Reviews*, 192(1-4), 237–283. <https://doi.org/10.1007/s11214-015-0172-9>
- Bolton, S. J., Bagenal, F., Blanc, M., Cassidy, T., Chané, E., Jackman, C., et al. (2015). Jupiter's magnetosphere: Plasma sources and transport. *Space Science Reviews*, 192(1-4), 209–236. <https://doi.org/10.1007/s11214-015-0184-5>

Acknowledgments

We are grateful to Dr. Kenneth (KC) Hansen for his work that created an earlier version of the BATSRUS Jupiter model, on which this study is largely based. This work was supported by the NASA Earth and Space Science Fellowship (NESSF), Grant 80NSSC17K0604. The model data were obtained from simulations using the SWMF/BATSRUS code developed at the University of Michigan, which is publicly available online (<http://csem.engin.umich.edu/tools/swmf/>). The simulation runs were performed on the Pleiades supercomputer managed by the NASA Advanced Supercomputing (NAS) division and the Blue Waters supercomputer at the NCSA supported by the NSF.

- Bonfond, B., Gladstone, G. R., Grodent, D., Greathouse, T. K., Versteeg, M. H., Hue, V., et al. (2017). Morphology of the UV aurorae Jupiter during Junos first perijove observations. *Geophysical Research Letters*, *44*, 4463–4471. <https://doi.org/10.1002/2017GL073114>
- Chané, E., Palmaerts, B., & Radioti, A. (2018). Periodic shearing motions in the Jovian magnetosphere causing a localized peak in the main auroral emission close to noon. *Planetary and Space Science*, *158*, 110–117. <https://doi.org/10.1016/j.pss.2018.04.023>
- Chané, E., Saur, J., Keppens, R., & Poedts, S. (2017). How is the Jovian main auroral emission affected by the solar wind? *Journal of Geophysical Research: Space Physics*, *122*, 1960–1978. <https://doi.org/10.1002/2016JA023318>
- Chané, E., Saur, J., & Poedts, S. (2013). Modeling Jupiter's magnetosphere: Influence of the internal sources. *Journal of Geophysical Research: Space Physics*, *118*, 2157–2172. <https://doi.org/10.1002/jgra.50258>
- Clarke, J. T., Nichols, J., Gérard, J. C., Grodent, D., Hansen, K. C., Kurth, W., et al. (2009). Response of Jupiter's and Saturn's auroral activity to the solar wind. *Journal of Geophysical Research*, *114*, A05210. <https://doi.org/10.1029/2008JA013694>
- Connerney, J. E. P., Kotsiaros, S., Oliverson, R. J., Espley, J. R., Joergensen, J. L., Joergensen, P. S., et al. (2018). A new model of Jupiter's magnetic field from Juno's first nine orbits. *Geophysical Research Letters*, *45*, 2590–2596. <https://doi.org/10.1002/2018GL077312>
- Cowley, S. W. H., Badman, S. V., Imber, S. M., & Milan, S. E. (2008). Comment on "Jupiter: A fundamentally different magnetospheric interaction with the solar wind" by DJ McComas and F. Bagenal. *Geophysical Research Letters*, *35*, L10101. <https://doi.org/10.1029/2007GL032645>
- Cowley, S. W. H., & Bunce, E. J. (2001). Origin of the main auroral oval in Jupiter's coupled magnetosphere–ionosphere system. *Planetary and Space Science*, *49*(10–11), 1067–1088. [https://doi.org/10.1016/s0032-0633\(00\)00167-7](https://doi.org/10.1016/s0032-0633(00)00167-7)
- Cowley, S. W. H., & Bunce, E. J. (2003). Modulation of Jupiter's main auroral oval emissions by solar wind induced expansions and compressions of the magnetosphere. *Planetary and Space Science*, *51*(1), 57–79. [https://doi.org/10.1016/S0032-0633\(02\)00118-6](https://doi.org/10.1016/S0032-0633(02)00118-6)
- Cowley, S. W. H., Bunce, E. J., & Nichols, J. D. (2003). Origins of Jupiter's main oval auroral emissions. *Journal of Geophysical Research*, *108*(A4), 8002. <https://doi.org/10.1029/2002JA009329>
- Cowley, S. W. H., Bunce, E. J., Stallard, T. S., & Miller, S. (2003). Jupiter's polar ionospheric flows: Theoretical interpretation. *Geophysical Research Letters*, *30*(5), 1220. <https://doi.org/10.1029/2002GL016030>
- Cowley, S. W. H., Nichols, J. D., & Andrews, D. J. (2007). Modulation of Jupiter's plasma flow, polar currents, and auroral precipitation by solar wind-induced compressions and expansions of the magnetosphere: a simple theoretical model. *Annals of Geophysics*, *25*(6), 1433–1463. <https://doi.org/10.5194/angeo-25-1433-2007>
- Crooker, N. U., Luhmann, J. G., Russell, C. T., Smith, E. J., Spreiter, J. R., & Stahara, S. S. (1985). Magnetic field draping against the dayside magnetopause. *Journal of Geophysical Research*, *90*(A4), 3505–3510. <https://doi.org/10.1029/JA090iA04p03505>
- Dougherty, L. P., Bodisch, K. M., & Bagenal, F. (2017). Survey of Voyager plasma science ions at Jupiter: 2. Heavy ions. *Journal of Geophysical Research: Space Physics*, *122*, 8257–8276. <https://doi.org/10.1002/2017JA024053>
- Dungey, J. W. (1961). Interplanetary magnetic field and the auroral zones. *Physical Review Letters*, *6*(2), 47–48. <https://doi.org/10.1103/PhysRevLett.6.47>
- Erkaev, N. V., Farrugia, C. J., & Biernat, H. K. (1996). Effects on the Jovian magnetosheath arising from solar wind flow around nonaxisymmetric bodies. *Journal of Geophysical Research*, *101*(A5), 10665–10672. <https://doi.org/10.1029/95JA03518>
- Farrugia, C. J., Biernat, H. K., & Erkaev, N. V. (1998). The effect of the magnetopause shapes of Jupiter and Saturn on magnetosheath parameters. *Planetary and Space Science*, *46*(5), 507–514. [https://doi.org/10.1016/S0032-0633\(97\)00225-0](https://doi.org/10.1016/S0032-0633(97)00225-0)
- Frank, L. A., Paterson, W. R., & Khurana, K. K. (2002). Observations of thermal plasmas in Jupiter's magnetotail. *Journal of Geophysical Research*, *107*(A1), 1003. <https://doi.org/10.1029/2001JA000077>
- Fukazawa, K., Ogino, T., & Walker, R. J. (2006). Configuration and dynamics of the Jovian magnetosphere. *Journal of Geophysical Research*, *111*, A10207. <https://doi.org/10.1029/2006JA011874>
- Fukazawa, K., Ogino, T., & Walker, R. J. (2005). Dynamics of the Jovian magnetosphere for northward interplanetary magnetic field (IMF). *Geophysical Research Letters*, *32*, L03202. <https://doi.org/10.1029/2004gl021392>
- Fukazawa, K., Ogino, T., & Walker, R. J. (2010). A simulation study of dynamics in the distant Jovian magnetotail. *Journal of Geophysical Research*, *115*, A09219. <https://doi.org/10.1029/2009JA015228>
- Gombosi, T. I., Tóth, G., De Zeeuw, D. L., Hansen, K. C., Kabin, K., & Powell, K. G. (2002). Semirelativistic magnetohydrodynamics and physics-based convergence acceleration. *Journal of Computational Physics*, *177*(1), 176–205. <https://doi.org/10.1006/jcph.2002.7009>
- Grodent, D. (2015). A brief review of ultraviolet auroral emissions on giant planets. *Space Science Reviews*, *187*(1–4), 23–50. <https://doi.org/10.1007/s11214-014-0052-8>
- Grodent, D., Clarke, J. T., Waite, J. H. Jr., Cowley, S. W. H., Gerard, J.-C., & Kim, J. (2003). Jupiter's polar auroral emissions. *Journal of Geophysical Research*, *108*(A10), 1366. <https://doi.org/10.1029/2003JA010017>
- Gurnett, D. A., Kurth, W. S., Hospodarsky, G. B., Persoon, A. M., Zarka, P., Lecacheux, A., et al. (2002). Control of Jupiter's radio emission and aurorae by the solar wind. *Nature*, *415*(6875), 985–987. <https://doi.org/10.1038/415985a>
- Hansen K. C., (2001). MHD Simulations of the magnetospheres of Jupiter and Saturn: Application to the Cassini mission. *PhD Thesis, University of Michigan – Ann Arbor*
- Hill, T. W. (1979). Inertial limit on corotation. *Journal of Geophysical Research*, *84*(A11), 6554–6558. <https://doi.org/10.1029/JA084iA11p06554>
- Hill, T. W. (1980). Corotation lag in Jupiter's magnetosphere: Comparison of observation and theory. *Science*, *207*(4428), 301–302. <https://doi.org/10.1126/science.207.4428.301>
- Hill, T. W. (2001). The Jovian auroral oval. *Journal of Geophysical Research*, *106*(A5), 8101–8107. <https://doi.org/10.1029/2000JA000302>
- Jia, X., Hansen, K. C., Gombosi, T. I., Kivelson, M. G., Tóth, G., DeZeeuw, D. L., & Ridley, A. J. (2012). Magnetospheric configuration and dynamics of Saturn's magnetosphere: A global MHD simulation. *Journal of Geophysical Research*, *117*, A05225. <https://doi.org/10.1029/2012JA017575>
- Jia, X., Kivelson, M. G., & Gombosi, T. I. (2012). Driving Saturn's magnetospheric periodicities from the atmosphere/ionosphere. *Journal of Geophysical Research*, *117*, A04215. <https://doi.org/10.1029/2011JA017367>
- Joy, S. P., Kivelson, M. G., Walker, R. J., Khurana, K. K., Russell, C. T., & Ogino, T. (2002). Probabilistic models of the Jovian magnetopause and bow shock locations. *Journal of Geophysical Research*, *107*(A10), 1309. <https://doi.org/10.1029/2001JA009146>
- Khurana, K. K. (2001). Influence of solar wind on Jupiter's magnetosphere deduced from currents in the equatorial plane. *Journal of Geophysical Research*, *106*(A11), 25999–26016. <https://doi.org/10.1029/2000JA000352>
- Khurana, K. K., Kivelson, M. G., Vasiliunas, V. M., Krupp, N., Woch, J., Lagg, A., et al. (2004). The configuration of Jupiter's magnetosphere. In F. Bagenal, T. E. Dowling, & W. B. McKinnon (Eds.), *Jupiter: The Planet, Satellites and Magnetosphere*, (pp. 593–616). Cambridge, UK: Cambridge University Press.

- Khurana, K. K., & Schwarzl, H. K. (2005). Global structure of Jupiter's magnetospheric current sheet. *Journal of Geophysical Research*, *110*, A07227. <https://doi.org/10.1029/2004JA010757>
- Kimura, T., Badman, S. V., Tao, C., Yoshioka, K., Murakami, G., Yamazaki, A., et al. (2015). Transient internally driven aurora at Jupiter discovered by Hisaki and the Hubble Space Telescope. *Geophysical Research Letters*, *42*, 1662–1668. <https://doi.org/10.1002/2015GL063272>
- Kimura, T., Hiraki, Y., Tao, C., Tsuchiya, F., Delamere, P. A., Yoshioka, K., et al. (2018). Response of Jupiter's aurora to plasma mass loading rate monitored by the Hisaki satellite during volcanic eruptions at Io. *Journal of Geophysical Research: Space Physics*, *123*, 1885–1899. <https://doi.org/10.1002/2017JA025029>
- Kimura, T., Nichols, J. D., Gray, R. L., Tao, C., Murakami, G., Yamazaki, A., et al. (2017). Transient brightening of Jupiter's aurora observed by the Hisaki satellite and Hubble Space Telescope during approach phase of the Juno spacecraft. *Geophysical Research Letters*, *44*, 4523–4531. <https://doi.org/10.1002/2017GL072912>
- Kita, H., Kimura, T., Tao, C., Tsuchiya, F., Misawa, H., Sakanoi, T., et al. (2016). Characteristics of solar wind control on Jovian UV auroral activity deciphered by long-term Hisaki EXCEED observations: Evidence of preconditioning of the magnetosphere? *Geophysical Research Letters*, *43*, 6790–6798. <https://doi.org/10.1002/2016GL069481>
- Kivelson, M. G., & Khurana, K. K. (2002). Properties of the magnetic field in the Jovian magnetotail. *Journal of Geophysical Research*, *107*(A8), 1196. <https://doi.org/10.1029/2001JA000249>
- Krupp, N., Vasyliunas, V., Woch, J., Lagg, A., Khurana, K., Kivelson, M., et al. (2004). Dynamics of the Jovian magnetosphere. In F. Bagenal, T. E. Dowling, & W. B. McKinnon (Eds.), *Jupiter: The planet, satellites and magnetosphere*, (pp. 617–638). Cambridge, UK: Cambridge University Press.
- Linde, T. (2002). A practical, general-purpose, two-state HLL Riemann solver for hyperbolic conservation laws. *International Journal for Numerical Methods in Fluids*, *40*(3–4), 391–402. <https://doi.org/10.1002/flid.312>
- Masters, A. (2017). Model-based assessments of magnetic reconnection and Kelvin-Helmholtz instability at Jupiter's magnetopause. *Journal of Geophysical Research: Space Physics*, *122*, 11,154–11,174. <https://doi.org/10.1002/2017JA024736>
- Mauk, B. H., Mitchell, D. G., McEntire, R. W., Paranicas, C. P., Roelof, E. C., Williams, D. J., et al. (2004). Energetic ion characteristics and neutral gas interactions in Jupiter's magnetosphere. *Journal of Geophysical Research*, *109*, A09S12. <https://doi.org/10.1029/2003JA010270>
- McComas, D. J., Allegrini, F., Bagenal, F., Cray, F., Ebert, R. W., Elliott, H., et al. (2007). Diverse plasma populations and structures in Jupiter's magnetotail. *Science*, *318*(5848), 217–220. <https://doi.org/10.1126/science.1147393>
- McComas, D. J., & Bagenal, F. (2007). Jupiter: A fundamentally different magnetospheric interaction with the solar wind. *Geophysical Research Letters*, *34*, L20106. <https://doi.org/10.1029/2007GL031078>
- Miyoshi, T., & Kusano, K. (1997). MHD simulation of a rapidly rotating magnetosphere interacting with the external plasma flow. *Geophysical Research Letters*, *24*(21), 2627–2630. <https://doi.org/10.1029/97GL52739>
- Moriguchi, T., Nakamizo, A., Tanaka, T., Obara, T., & Shimazu, H. (2008). Current systems in the Jovian magnetosphere. *Journal of Geophysical Research*, *113*, A05204. <https://doi.org/10.1029/2007JA012751>
- Nichols, J. D. (2011). Magnetosphere-ionosphere coupling in Jupiter's middle magnetosphere: Computations including a self-consistent current sheet magnetic field model. *Journal of Geophysical Research*, *116*, A10232. <https://doi.org/10.1029/2011JA016922>
- Nichols, J. D., Badman, S. V., Bagenal, F., Bolton, S. J., Bonfond, B., Bunce, E. J., et al. (2017). Response of Jupiter's auroras to conditions in the interplanetary medium as measured by the Hubble Space Telescope and Juno. *Geophysical Research Letters*, *44*, 7643–7652. <https://doi.org/10.1002/2017GL073029>
- Nichols, J. D., Bunce, E. J., Clarke, J. T., Cowley, S. W. H., Gérard, J. C., Grodent, D., & Pryor, W. R. (2007). Response of Jupiter's UV auroras to interplanetary conditions as observed by the Hubble Space Telescope during the Cassini flyby campaign. *Journal of Geophysical Research*, *112*, A02203. <https://doi.org/10.1029/2006JA012005>
- Nichols, J. D., Clarke, J. T., Gérard, J. C., & Grodent, D. (2009). Observations of Jovian polar auroral filaments. *Geophysical Research Letters*, *36*, L08101. <https://doi.org/10.1029/2009GL037578>
- Nichols, J. D., & Cowley, S. W. H. (2003). Magnetosphere-ionosphere coupling currents in Jupiter's middle magnetosphere: Dependence on the effective ionospheric Pedersen conductivity and iogenic plasma mass outflow rate. *Annals of Geophysics*, *21*, 1419–1441. <https://doi.org/10.5194/angeo-21-1419-2003>
- Nichols, J. D., & Cowley, S. W. H. (2004). Magnetosphere-ionosphere coupling currents in Jupiter's middle magnetosphere: Effect of precipitation-induced enhancement of the ionospheric Pedersen conductivity. *Annals of Geophysics*, *22*(5), 1799–1827. <https://doi.org/10.5194/angeo-22-1799-2004>
- Nichols, J. D., Cowley, S. W. H., & McComas, D. J. (2006). Magnetopause reconnection rate estimates for Jupiter's magnetosphere based on interplanetary measurements at ~5AU. *Annales Geophysicae*, *24*(1), 393–406. <https://doi.org/10.5194/angeo-24-393-2006>
- Ogino, T., Walker, R. J., & Kivelson, M. G. (1998). A global magnetohydrodynamic simulation of the Jovian magnetosphere. *Journal of Geophysical Research*, *103*(A1), 225–235. <https://doi.org/10.1029/97JA02247>
- Pontius, D. H. Jr. (1997). Radial mass transport and rotational dynamics. *Journal of Geophysical Research*, *102*(A4), 7137–7150. <https://doi.org/10.1029/97JA00289>
- Powell, K. G., Roe, P. L., Linde, T. J., Gombosi, T. I., & De Zeeuw, D. L. (1999). A solution-adaptive upwind scheme for ideal magnetohydrodynamics. *Journal of Computational Physics*, *154*(2), 284–309. <https://doi.org/10.1006/jcph.1999.6299>
- Ridley, A. J., Gombosi, T. I., & DeZeeuw, D. L. (2004). Ionospheric control of the magnetosphere: conductance. *Annales Geophysicae*, *22*(2), 567–584. <https://doi.org/10.5194/angeo-22-567-2004>
- Schreier, R., Eviatar, A., & Vasyliunas, V. M. (1998). A two-dimensional model of plasma transport and chemistry in the Jovian magnetosphere. *Journal of Geophysical Research*, *103*(E9), 19901–19913. <https://doi.org/10.1029/98JE00697>
- Slavin, J. A., Smith, E. J., Spreiter, J. R., & Stahara, S. S. (1985). Solar wind flow about the outer planets: Gas dynamic modeling of the Jupiter and Saturn bow shocks. *Journal of Geophysical Research*, *90*(A7), 6275–6286. <https://doi.org/10.1029/JA090iA07p06275>
- Southwood, D. J., & Kivelson, M. G. (2001). A new perspective concerning the influence of the solar wind on the Jovian magnetosphere. *Journal of Geophysical Research*, *106*(A4), 6123–6130. <https://doi.org/10.1029/2000JA000236>
- Strobel, D., & Atreya, S. (1983). Ionosphere. In A. Dessler (Ed.), *Physics of the Jovian magnetosphere*, Cambridge Planetary Science Old, (pp. 51–67). Cambridge: Cambridge University Press. <https://doi.org/10.1017/CBO9780511564574.004>
- Sulaiman, A. H., Jia, X., Achilleos, N., Sergis, N., Gurnett, D. A., & Kurth, W. S. (2017). Large-scale solar wind flow around Saturn's non-axisymmetric magnetosphere. *Journal of Geophysical Research: Space Physics*, *122*, 9198–9206. <https://doi.org/10.1002/2017JA024595>
- Sulaiman, A. H., Masters, A., Dougherty, M. K., & Jia, X. (2014). The magnetic structure of Saturn's magnetosheath. *Journal of Geophysical Research: Space Physics*, *119*, 5651–5661. <https://doi.org/10.1002/2014JA020019>

- Tao, C., Kataoka, R., Fukunishi, H., Takahashi, Y., & Yokoyama, T. (2005). Magnetic field variations in the Jovian magnetotail induced by solar wind dynamic pressure enhancements. *Journal of Geophysical Research*, *110*, A11208. <https://doi.org/10.1029/2004JA010959>
- Tóth, G., De Zeeuw, D. L., Gombosi, T. I., & Powell, K. G. (2006). A parallel explicit/implicit time stepping scheme on block-adaptive grids. *Journal of Computational Physics*, *217*(2), 722–758. <https://doi.org/10.1016/j.jcp.2006.01.029>
- Tóth, G., Meng, X., Gombosi, T. I., & Ridley, A. J. (2011). Reducing numerical diffusion in magnetospheric simulations. *Journal of Geophysical Research*, *116*, A07211. <https://doi.org/10.1029/2010JA016370>
- Tóth, G., van der Holst, B., Sokolov, I. V., de Zeeuw, D. L., Gombosi, T. I., Fang, F., et al. (2012). Adaptive numerical algorithms in space weather modeling. *Journal of Computational Physics*, *231*(3), 870–903. <https://doi.org/10.1016/j.jcp.2011.02.006>
- Vasyliunas, V. M. (1983). Plasma distribution and flow. *Physics of the Jovian Magnetosphere*, 395–453. <https://doi.org/10.1017/CBO9780511564574.013>
- Vogt, M. F., Jackman, C. M., Slavin, J. A., Bunce, E. J., Cowley, S. W. H., Kivelson, M. G., & Khurana, K. K. (2014). Structure and statistical properties of plasmoids in Jupiter's magnetotail. *Journal of Geophysical Research: Space Physics*, *119*, 821–843. <https://doi.org/10.1002/2013JA019393>
- Vogt, M. F., Kivelson, M. G., Khurana, K. K., Joy, S. P., & Walker, R. J. (2010). Reconnection and flows in the Jovian magnetotail as inferred from magnetometer observations. *Journal of Geophysical Research*, *115*, A06219. <https://doi.org/10.1029/2009JA015098>
- Vogt, M. F., Kivelson, M. G., Khurana, K. K., Walker, R. J., Bonfond, B., Grodent, D., & Radioti, A. (2011). Improved mapping of Jupiter's auroral features to magnetospheric sources. *Journal of Geophysical Research*, *116*, A03220. <https://doi.org/10.1029/2010JA016148>
- Walker, R. J., & Jia, X. (2016). Simulation studies of plasma transport at Earth, Jupiter and Saturn. In W. Gonzalez, & E. Parker (Eds.), *Magnetic reconnection*. (pp. 345–372, Vol. 427) Springer. https://doi.org/10.1007/978-3-319-26432-5_9
- Walker, R. J., Ogino, T., & Kivelson, M. G. (2001). Magnetohydrodynamic simulations of the effects of the solar wind on the Jovian magnetosphere. *Planetary and Space Science*, *49*(3–4), 237–245. [https://doi.org/10.1016/S0032-0633\(00\)00145-8](https://doi.org/10.1016/S0032-0633(00)00145-8)
- Wang, Y., Guo, X., Tang, B., Li, W., & Wang, C. (2018). Modeling the Jovian magnetosphere under an antiparallel interplanetary magnetic field from a global MHD simulation. *Earth and Planetary Physics*, *2*, 303–309. <https://doi.org/10.26464/epp2018028>
- Wilson, R. J., Bagenal, F., Valek, P. W., McComas, D. J., Allegrini, F., Ebert, R. W., et al. (2018). Solar wind properties during Juno's approach to Jupiter: Data analysis and resulting plasma properties utilizing a 1-D forward model. *Journal of Geophysical Research: Space Physics*, *123*, 2772–2786. <https://doi.org/10.1002/2017JA024860>
- Woch, J., Krupp, N., & Lagg, A. (2002). Particle bursts in the Jovian magnetosphere: Evidence for a near-Jupiter neutral line. *Geophysical Research Letters*, *29*(7), 1138. <https://doi.org/10.1029/2001GL014080>
- Zieger, B., & Hansen, K. C. (2008). Statistical validation of a solar wind propagation model from 1 to 10 AU. *Journal of Geophysical Research*, *113*, A08107. <https://doi.org/10.1029/2008JA013046>